Roughness-induced streaming in turbulent wave boundary layers

Fuhrman, David R.; Sumer, B. Mutlu; Fredsøe, Jørgen

Published in:
Journal of Geophysical Research: Atmospheres

Link to article, DOI:
10.1029/2011JC007155

Publication date:
2011

Document Version
Publisher's PDF, also known as Version of record

Roughness-induced streaming in turbulent wave boundary layers

David R. Fuhrman,[1] B. Mutlu Sumer,[1] and Jørgen Fredsøe[1]

Received 21 March 2011; revised 28 June 2011; accepted 11 July 2011; published 1 October 2011.

[1] A comprehensive numerical study of oscillatory wave boundary layers on spatially varying bottom roughness is presented. The study utilizes a model solving incompressible Reynolds-averaged Navier-Stokes equations coupled with k-ω turbulence closure, modified in a simple way to incorporate anisotropy in turbulent normal stresses. The model is first validated via comparison with existing oscillating tunnel measurements involving sudden bottom roughness transitions. It is then used to parametrically study oscillatory boundary layer flows, wherein the bed shear stress amplifications and period-averaged streaming characteristics induced by bottom roughness variations are systematically assessed. The effects of variable roughness ratio, gradual roughness transitions, as well as changing flow orientation in plan are all considered. As part of the latter, roughness-induced secondary flows are predicted to occur as the oscillatory flow becomes oriented parallel to a line of roughness transition. This phenomenon is proposed as a natural transverse grain sorting mechanism for coastal flows over graded sediments. Subsequent model testing demonstrates potential generation of secondary circulation cells having characteristic size the order of the wave boundary layer thickness. Analogy is made to similar features known to develop within steady flows, having characteristic size the order of the flow depth.

Citation: Fuhrman, D. R., B. M. Sumer, and J. Fredsøe (2011), Roughness-induced streaming in turbulent wave boundary layers, *J. Geophys. Res.*, *116*, C10002, doi:10.1029/2011JC007155.

1. Introduction

[2] The effects of surface roughness transitions on steady turbulent boundary layers have been extensively studied experimentally, numerically, and theoretically. Such investigations have historically been within the context of atmospheric boundary layers, and include, e.g., *Townsend* [1966], *Taylor* [1969], *Blom and Wartena* [1969], *Antonia and Luxton* [1971, 1972], *Shir* [1972], *Rao et al.* [1974], *Schofield* [1975], *Jensen* [1978], *Andreopoulos and Wood* [1982], *Belcher et al.* [1990], *Beljaars et al.* [1990], *Wright et al.* [1998], and *Chan* [2001]. *Chen and Chiew* [2003] have additionally studied the problem of a step change in bottom roughness within open channel flow.

[3] The study of unsteady turbulent oscillatory wave boundary layers, on the other hand, has primarily focused on problems involving spatially uniform bottom roughness. These include experimental [e.g., *Sleath*, 1987, 1988; *Jensen et al.*, 1989], numerical [e.g., *Justesen*, 1988; *Holmedal and Myrhaug*, 2009], as well as theoretical [e.g., *Grant and Madsen*, 1979; *Myrhaug*, 1982; *Myrhaug and Slaattelid*, 1989; *Fredsøe*, 1984; *Foster et al.*, 1999] investigations, just to mention a few. Comparatively little is known on the effects of spatial non-uniformity of any kind. Spatial non-uniformity induced by sloping bed effects has e.g. been studied experimentally by *Sumer et al.* [1993], numerically by *Fuhrman et al.* [2009a, 2009b], and theoretically and in the field by *Zou and Hay* [2003] and *Zou et al.* [2003]. Studies focusing on the specific effects of bottom roughness transition on oscillatory boundary layers, the focus of the present work, appear limited to *Fredsøe et al.* [1993], who conducted oscillatory tunnel experiments involving sudden transitions, and *Laursen et al.* [1994], who utilized a numerical one-dimensional Lagrangian description, wherein the bottom roughness was abruptly changed in time.

[4] Further understanding of the specific effects of bottom roughness transitions on oscillatory flows is important for two principal reasons. First, these effects are of engineering interest, having obvious relevance to flow around stone protection layers, commonly used for scour protection at the base of coastal structures. Such effects are likewise of geophysical interest, with relevance to coastal flows over naturally (or otherwise) graded sediments. The present work will add to existing knowledge on this subject by conducting a numerical study on the effects of spatially varying bottom roughness on oscillatory wave boundary layers. For this purpose, problems involving bottom roughness transition will be resolved directly in two spatial dimensions, hence improving on the earlier numerical study by *Laursen et al.* [1994]. New aspects not previously considered will also be investigated. These will include effects of gradual (rather than sudden) roughness transition, as well as those associated with changing flow orientation in plan. The latter is particularly important, given e.g. that the stone-sand border within a stone protection layer will inevitably meet waves at

[1]Department of Mechanical Engineering, Technical University of Denmark, Kongens Lyngby, Denmark.

0148-0227/11/2011JC007155

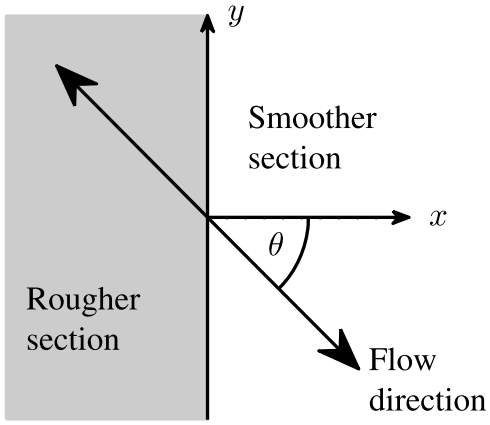

Figure 1. Definition sketch (in plan) illustrating oscillatory flow with arbitrary flow direction θ.

all attacking angles. Particular emphasis will be placed on studying bed shear stress amplifications and period-averaged streaming characteristics. Through physical reasoning, when relevant, the study additionally aims to shed light on potential natural grain sorting mechanisms associated with these processes.

[5] The paper is organized as follows: The numerical model utilized is presented in section 2, and validated against experimental measurements by *Fredsøe et al.* [1993] in section 3. Parametric study of oscillatory flows normal to transitional roughness follows in section 4, wherein both sudden (section 4.1) and gradual roughness transitions (section 4.2) are considered. Oblique oscillatory flows, demonstrating effects of changing flow orientation in plan, are then considered in section 5, with features associated with predicted secondary transverse flows studied in more detail in section 6. Conclusions are finally drawn in section 7.

2. The Numerical Model

[6] In this section a description of the computational model used throughout the present work is provided. The numerical model solves the incompressible Reynolds-averaged Navier-Stokes equations

$$\frac{\partial u_i}{\partial t} + u_j \frac{\partial u_i}{\partial x_j} = -\frac{1}{\rho}\frac{\partial p}{\partial x_i} + \frac{\partial}{\partial x_j}\left[2\nu S_{ij} + \frac{\tau_{ij}}{\rho}\right] + B_i, \tag{1}$$

where the mean-strain-rate tensor is

$$S_{ij} = \frac{1}{2}\left(\frac{\partial u_i}{\partial x_j} + \frac{\partial u_j}{\partial x_i}\right). \tag{2}$$

This is combined with the local continuity equation

$$\frac{\partial u_i}{\partial x_i} = 0. \tag{3}$$

Here u_i are the mean (phase-resolved) velocities, x_i are the Cartesian coordinates, t is time, p is the static pressure, ν is the fluid kinematic viscosity, ρ is the fluid density, and τ_{ij} is the Reynolds stress tensor, which accounts for additional (normal and shear) stresses due to momentum transfer from turbulent fluctuations. In (1) B_i represents body forces used to drive the flow. In what follows (unless otherwise stated), these are specified according to

$$(B_1, B_2, B_3) = (\cos\theta, \sin\theta, 0) U_{1m}\omega\cos(\omega t), \tag{4}$$

which drives a sinusoidally varying free stream velocity field of the form

$$(u_1, u_2, u_3) = (u, v, w) = (\cos\theta, \sin\theta, 0) U_{1m}\sin(\omega t), \tag{5}$$

having maximum velocity U_{1m} and angular frequency $\omega = 2\pi/T$, where T is the wave period. The velocities u and v are assumed to be in the horizontal x- and y-directions, respectively, whereas w is assumed to be in the vertical z-direction. In what follows, spatial variations in bottom roughness will be considered in the x-direction only. Hence θ defines the forced flow direction relative to the line of roughness transition, as depicted conceptually in Figure 1. As the described problem is invariant with respect to the y-direction, it conveniently remains two-dimensional in nature, though problems with $\theta \neq 0°$ will give rise to mean velocities in all three spatial directions. Unless otherwise stated $\theta = 0°$, i.e. body forcing is applied only in the pure x-direction.

[7] Throughout the present work the Reynolds stress tensor will be defined according to the constitutive relation

$$\frac{\tau_{ij}}{\rho} = -\overline{u_i' u_j'} = 2\nu_T S_{ij} - a_{(i)} k \delta_{ij}, \tag{6}$$

where δ_{ij} is the Kronecker delta, ν_T is the eddy viscosity,

$$k = \frac{1}{2}\overline{u_i' u_i'} \tag{7}$$

is the turbulent kinetic energy density, and the overbar denotes time averaging. Note that in (6) the subscript in parentheses (i) indicates suppressed summation over this particular index. The $a_{(i)}$ coefficients are defined as a function of the forced flow direction θ according to

$$\left(a_{(1)}, a_{(2)}, a_{(3)}\right) = \left(\frac{8}{9}\cos^2\theta + \frac{2}{3}\sin^2\theta, \frac{2}{3}\cos^2\theta + \frac{8}{9}\sin^2\theta, \frac{4}{9}\right). \tag{8}$$

These relations are selected to guarantee fixed 4:3:2 ratios for the streamwise, transverse, and vertical fluctuating velocity components, respectively, at the limit of spatially uniform flow (see the derivation in Appendix A). As an example, for uniform flow with $\theta = 0°$ (i.e. streamwise flow in the x-direction) the present model predicts

$$-\frac{\tau_{11}}{\rho} = \overline{u'^2} = \frac{8}{9}k, \tag{9}$$

$$-\frac{\tau_{22}}{\rho} = \overline{v'^2} = \frac{2}{3}k, \tag{10}$$

$$-\frac{\tau_{33}}{\rho} = \overline{w'^2} = \frac{4}{9}k. \tag{11}$$

Alternatively, with $\theta = 90°$ (i.e. streamwise flow in the y-direction) it yields

$$-\frac{\tau_{11}}{\rho} = \overline{u'^2} = \frac{2}{3}k, \tag{12}$$

$$-\frac{\tau_{22}}{\rho} = \overline{v'^2} = \frac{8}{9}k, \tag{13}$$

$$-\frac{\tau_{33}}{\rho} = \overline{w'^2} = \frac{4}{9}k. \tag{14}$$

These fixed ratios are known to be a good approximation throughout the log layer and much of the defect layer within flat-plate boundary layers [*Wilcox*, 2006, p. 309]. The 2:1 ratio for streamwise-to-vertical fluctuating components is likewise reasonably in line with steady uniform flow data over rough beds collected by *Grass* [1971].

[8] Hence, by adopting (8) the present model will, in a simple way, provide anisotropic turbulent normal stresses that are consistent with known uniform channel flow characteristics. This is in contrast to the traditionally-used standard Boussinesq approximation, which simply utilizes constant $a_{(i)} = 2/3$. Note also that, as the coefficients in (8) sum to 2 for all θ, the relation (7) is inherently satisfied, which can readily be seen by taking the trace of (6) and invoking (3). The off-diagonal (shear) components of the Reynolds stress tensor, on the other hand, are left to be modeled in the standard way.

[9] It should be stressed that the use of (8) assumes clear distinction between (known) streamwise, transverse, and vertical directions, with the vertical z-direction assumed normal to wall boundaries. Hence, it is not valid e.g. where side-wall or corner effects are important; These would require nonlinear constitutive relations [e.g., *Speziale*, 1987; *Wilcox*, 2006, pp. 308–311] e.g. for the prediction of secondary flows arising in non-circular pipes. This is not an issue in the present work, however, which will utilize periodic conditions at all horizontal boundaries. Hence, the advantage of the present approach lies merely in its simplicity for the particular idealized flow configurations considered, at the expense of greater generality offered by other, more complicated, anisotropic approaches. As will be demonstrated in later sections, the present model is capable of predicting secondary flows induced by periodically connected regions having variable bottom roughness.

[10] To achieve closure, we adopt the two-equation k-ω turbulence model of *Wilcox* [2006, 2008]. In this model the eddy viscosity is defined by

$$\nu_T = \frac{k}{\tilde{\omega}}, \qquad \tilde{\omega} = \max\left\{\omega, C_{lim}\sqrt{\frac{2S_{ij}S_{ij}}{\beta^*}}\right\}, \tag{15}$$

which incorporates a stress limiting feature, with $C_{lim} = 7/8$. This model additionally utilizes a transport equation for the turbulent kinetic energy density k

$$\frac{\partial k}{\partial t} + u_j\frac{\partial k}{\partial x_j} = \frac{\tau_{ij}}{\rho}\frac{\partial u_i}{\partial x_j} - \beta^* k\omega + \frac{\partial}{\partial x_j}\left[\left(\nu + \sigma^*\frac{k}{\omega}\right)\frac{\partial k}{\partial x_j}\right], \tag{16}$$

and a transport equation for the specific dissipation rate ω

$$\frac{\partial \omega}{\partial t} + u_j\frac{\partial \omega}{\partial x_j} = \alpha\frac{\omega}{k}\frac{\tau_{ij}}{\rho}\frac{\partial u_i}{\partial x_j} - \beta\omega^2 + \frac{\sigma_d}{\omega}\frac{\partial k}{\partial x_j}\frac{\partial \omega}{\partial x_j} + \frac{\partial}{\partial x_j}\left[\left(\nu + \sigma\frac{k}{\omega}\right)\frac{\partial \omega}{\partial x_j}\right], \tag{17}$$

where

$$\sigma_d = \mathcal{H}\left\{\frac{\partial k}{\partial x_j}\frac{\partial \omega}{\partial x_j}\right\}\sigma_{do}, \tag{18}$$

and $\mathcal{H}\{\cdot\}$ is the Heaviside step function, taking a value of zero when the argument is negative, and a value of unity otherwise. The standard model closure coefficients are used: $\alpha = 13/25$, $\beta = \beta_0 f_\beta$, $\beta_0 = 0.0708$, $\beta^* = 9/100$, $\sigma = 1/2$, $\sigma^* = 3/5$, and $\sigma_{do} = 1/8$. Note that for two-dimensional problems, as considered throughout the present work, $f_\beta = 1$ and hence $\beta = \beta_0$. For the generalization to three spatial dimensions see *Wilcox* [2006].

[11] The model is subject to the following wall boundary conditions: At friction wall boundaries a no-slip condition is imposed whereby all mean velocity variables are set to zero. Additionally, a zero normal gradient condition is imposed for k i.e. $\partial k/\partial z = 0$, corresponding to a zero flux of turbulent kinetic energy through the wall. This boundary condition for k was first used within k-ω modeling by *Roulund et al.* [2005], based on experimental evidence reported by *Sumer et al.* [2003]. More recently, *Fuhrman et al.* [2010] have demonstrated that this condition allows near bed grid spacing above hydraulically rough walls to be based on the roughness length, rather than a viscous length scale conventionally required with a $k = 0$ boundary condition. In the present work computational grids are stretched vertically such that the cell height nearest the bed Δz satisfies $\Delta z/k_N \leq 0.02$ for rough surfaces, where k_N is Nikuradse's equivalent sand grain roughness; and $\Delta z^+ = \Delta z U_{fm}/\nu \leq 1$ for smooth surfaces, where U_{fm} is the maximum friction velocity $U_f = \sqrt{|\tau_b|/\rho}$ occurring over the oscillatory period, with τ_b the bed shear stress. The rough bed constraint is in line with the criterion suggested by *Fuhrman et al.* [2010] for steady flow profiles, whereas the smooth bed constraint ensures resolution of a viscous sub-layer.

[12] The wall boundary condition for ω is specified according to [*Wilcox*, 2006]:

$$\omega = \frac{U_f^2}{\nu}S_R, \tag{19}$$

where the function S_R is defined as:

$$S_R = \begin{cases} \left(\dfrac{200}{k_N^+}\right)^2, & k_N^+ \leq 5 \\ \dfrac{180}{k_N^+} + \left[\left(\dfrac{200}{k_N^+}\right)^2 - \dfrac{180}{k_N^+}\right]e^{5-k_N^+}, & k_N^+ > 5. \end{cases} \tag{20}$$

Here $k_N^+ = k_N U_f/\nu$ is the roughness Reynolds number. This boundary condition is identical to that suggested by *Wilcox* [2006], with one exception: The rough-wall coefficient 180 in (20) was originally suggested to be 100 by *Wilcox* [2006]. This modification is necessitated by the switch to the

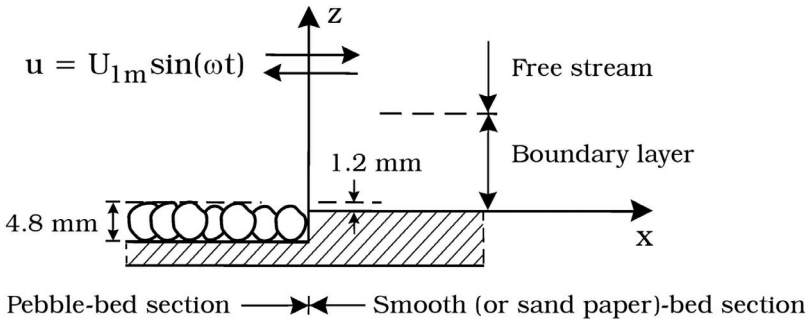

Figure 2. Conceptual sketch of the roughness change within the oscillating tunnel experiments of *Fredsøe et al.* [1993].

$\partial k/\partial z = 0$ boundary condition, as discussed by *Fuhrman et al.* [2010].

[13] The equations outlined above are solved numerically using the open-source CFD toolbox OpenFOAM® (OpenFOAM® is a registered trade mark of OpenCFD Limited, the producer of the OpenFOAM software), version 1.5, making use of a finite volume spatial discretization, in conjunction with a standard PISO algorithm. Dynamic time stepping is utilized, such that the internal Courant number is less than 0.2. Simulations involving oscillatory flows are run for 10 full periods, with the results shown corresponding to the final period, by which time the model is essentially in a periodically repetitive state.

3. Model Validation

3.1. Model Setup

[14] The model described above will first be validated against experimental measurements by *Fredsøe et al.* [1993], who performed a series of tests involving oscillatory wave boundary layer flows over beds having a sudden change in bottom roughness within an oscillating tunnel facility. In particular *Fredsøe et al.* [1993] made detailed measurements of period-averaged velocity profiles, bed shear stresses, and turbulence quantities, all of which will be compared against in what follows. A conceptual sketch showing their experimental configuration is shown in Figure 2. In the present work, a detailed model comparison will specifically be made against their experimental measurements for oscillatory flow over a pebble-smooth bed transition (their Test 1) and a pebble-sand paper transition (their Test 3), where the rougher pebble section in both cases will be considered as the left-hand section, as depicted in Figure 2. Apart from the roughness of the smoother (i.e. either smooth or sand-paper) right-hand section, the physical parameters used in these two experiments are similar, utilizing an oscillatory flow with period $T = 9.75$ s, with free stream velocity magnitude $U_{1m} \approx 2$ m/s, giving an amplitude of the free stream orbital motion $a = U_{1m}/\omega \approx 3$ m, again taking $\omega = 2\pi/T$ as the angular frequency. The precise parameters are summarized in detail within Table 1, which includes the grain sizes d as well as the roughness height k_N measured for each section by *Fredsøe et al.* [1993]. Note that throughout the present work base variables d and k_N will correspond to parameters on the rougher (left-hand) section, whereas variables having a prime superscript (d', k'_N) will correspond to the less-rough (right-hand) section.

[15] For comparison against these experiments the numerical model is set up using a four-block structure, as depicted in Figure 3, where the roughness transition occurs at the origin, and where the height of each block matches the tunnel half-depth $D = 0.145$ m. As seen there, the model domain is set up to utilize a large width of the two uniform-roughness sections $b = 12$ m ($\approx 3a$). This avoids any effects from the (poorly resolved) roughness change associated with the periodically connected left/right-hand boundaries from polluting the highly-resolved roughness transition in the middle of the domain. The grids within each block are stretched both horizontally and vertically to provide very high resolution of the boundary layer in the vicinity of the roughness change $x = 0$, as seen in Figure 3. The two lower blocks each consist of a 25×100 computational mesh, whereas the two top blocks each consist of a 25×50 mesh. The increased number of vertical cells within the bottom blocks was utilized to provide a finer resolution of the boundary layer where the roughness change occurs, as this is the area of principal interest. For the present simulations, both top and bottom walls are considered as friction walls, however, and both boundary layers are therefore resolved, to match the experimental conditions as closely as possible. It should be mentioned that, in an effort to match the vertical position of the theoretical bed for the two sections, *Fredsøe et al.* [1993] placed the (right-hand) smooth bed section a distance of $0.25d = 1.2$ mm below the top of the roughness elements of the pebble-bed section, as depicted in Figure 2. This is in accordance with steady boundary layer research of *Bayazit* [1976, 1983], who found that the theoretical wall on rough beds lies a distance of $0.15d$–$0.35d$ below the top

Table 1. Summary of Parameters From the Oscillatory Tunnel Experiments of *Fredsøe et al.* [1993][a]

Test	U_{1m} (m/s)	a (m)	d (m)	k_N (m)	d' (m)	$k'_N(m)$	$Re = aU_{1m}/\nu$	a/k_N	k_N/k'_N
1	1.97	3.04	0.0048	0.015	smooth	smooth	6×10^6	200	∞
3	2.05	3.18	0.0048	0.015	0.00035	0.00084	6.5×10^6	210	17.9

[a]Base variables (d, k_N) correspond to the left-hand (pebble covered) section, whereas those with prime superscripts (d, k_N) correspond to the right-hand (either smooth or sand paper covered) section. All tests use period $T = 9.75$ s.

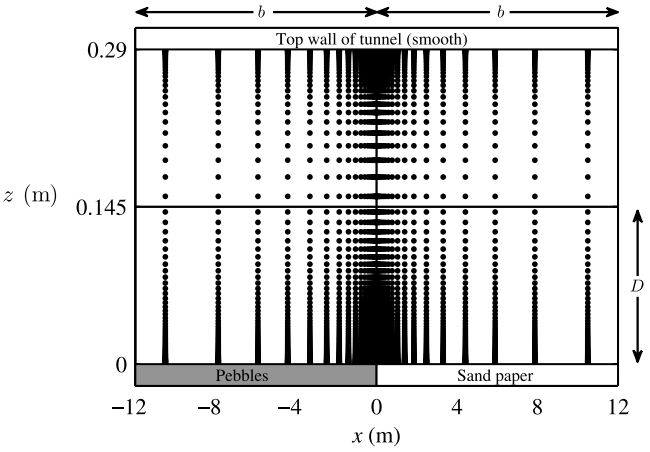

Figure 3. Example grid showing the four-block structure used for the simulation of Test 3 of *Fredsøe et al.* [1993], where the dots represent cell centers, and the full lines distinguish the blocks. Near the origin, the mesh uses $\Delta x/k_N = 0.2$, $\Delta y/k_N = 0.001$. Note that the vertical scale in this plot is grossly exaggerated.

of the roughness elements. Accordingly, the experimental conditions are modeled using a flat bottom along $z = 0$.

3.2. Period-Averaged Velocities

[16] We will begin the validation of the present model by comparing against measured period-averaged velocity profiles from *Fredsøe et al.* [1993]. As described therein, an oscillatory flow over a sudden change in roughness will result in differences between successive half-cycles in the vicinity of the roughness change. During the negative half-cycle, where the flow is directed toward the rougher section, the near-bed fluid leaving the smoother section will have unnaturally large velocity as it enters the rougher section, when compared to an otherwise similar flow over a bed having uniformly larger roughness k_N. Conversely, during the positive half-cycle (flow directed toward the smoother section), the near-bed flow coming off the rougher section will be characterized by reduced velocity gradients (and thereby velocities), when compared to flow over a uniformly smoother bottom (with roughness k'_N). These features are demonstrated quantitatively in Figure 4, which depicts the Test 1 horizontal velocity profiles averaged over both positive and negative half-cycles (denoted $\langle u\rangle^{\pm}$) at the location of the roughness change $x = 0$ (Figure 4a), as well as the resulting velocity profile averaged over the full period (denoted $\langle u\rangle$, Figure 4b). As can be seen the net result due to these described differences in the two half-cycles is a period-averaged near-bed flow in the direction of larger roughness, which will be referred to herein as roughness-induced "streaming". This flow is in turn seemingly compensated by a circulation current in the direction of the smoother section higher up in the profile, such that there is negligible net flow in the x-direction.

[17] Comparison of model results with the experimental measurements by *Fredsøe et al.* [1993] for the period-averaged horizontal velocity profiles is provided in Figure 5 at a number of positions in the vicinity of the roughness change. Both Test 1 (Figure 5, top) and Test 3 conditions (Figure 5, bottom) are considered. As can be seen, a reasonable match between the computed and measured profiles is achieved at all positions, for both tests. Both the computed and measured results suggest streaming velocities of $\langle u\rangle/U_{1m} = O(-0.1)$, where the negative sign indicates flow towards the larger roughness. Slightly reduced values are expectedly observed for the case involving pebble-to-sandpaper transition (Test 3), when compared to the more dramatic pebble-to-smooth bed transition (Test 1).

3.3. Turbulence Quantities

[18] We will now continue our investigation by comparing model results with measured turbulence quantities. *Fredsøe et al.* [1993] present measured (ensemble averaged) values of both root-mean-squared horizontal and vertical fluctuating velocities, as well as the Reynolds stress for their Test 1 conditions. In what follows we will specifically compare with their measured root-mean-squared horizontal fluctuating velocities $u'_{rms} = \sqrt{\overline{u'^2}}$, which can be expected to be the most significant contribution to the (square root of the) total turbulent kinetic energy density. We again note that, due to the use of (8), individual turbulence quantities, including leading-order anisotropy in the various fluctuating components, are provided directly from the present turbulence model. For example, for the present purposes, after taking $\theta = 0°$, (6) and (8) directly yield:

$$\overline{u'^2} = \frac{8}{9}k - 2\nu_T \frac{\partial u}{\partial x}, \tag{21}$$

$$\overline{v'^2} = \frac{2}{3}k - 2\nu_T \frac{\partial v}{\partial y}, \tag{22}$$

$$\overline{w'^2} = \frac{4}{9}k - 2\nu_T \frac{\partial w}{\partial z}. \tag{23}$$

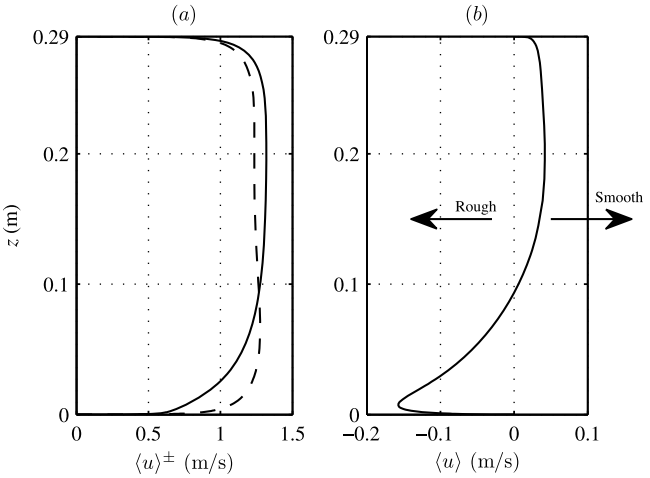

Figure 4. Computed horizontal velocity profiles at $x = 0$ for Test 1 of *Fredsøe et al.* [1993] averaged over (a) positive $\langle u\rangle^{+}$ (full line) and negative $\langle u\rangle^{-}$ (dashed line) half-periods, and (b) the full period $\langle u\rangle$. In Figure 4a the profile for the negative half-period (dashed line) is shown as positive, to ease comparison between the successive half-periods.

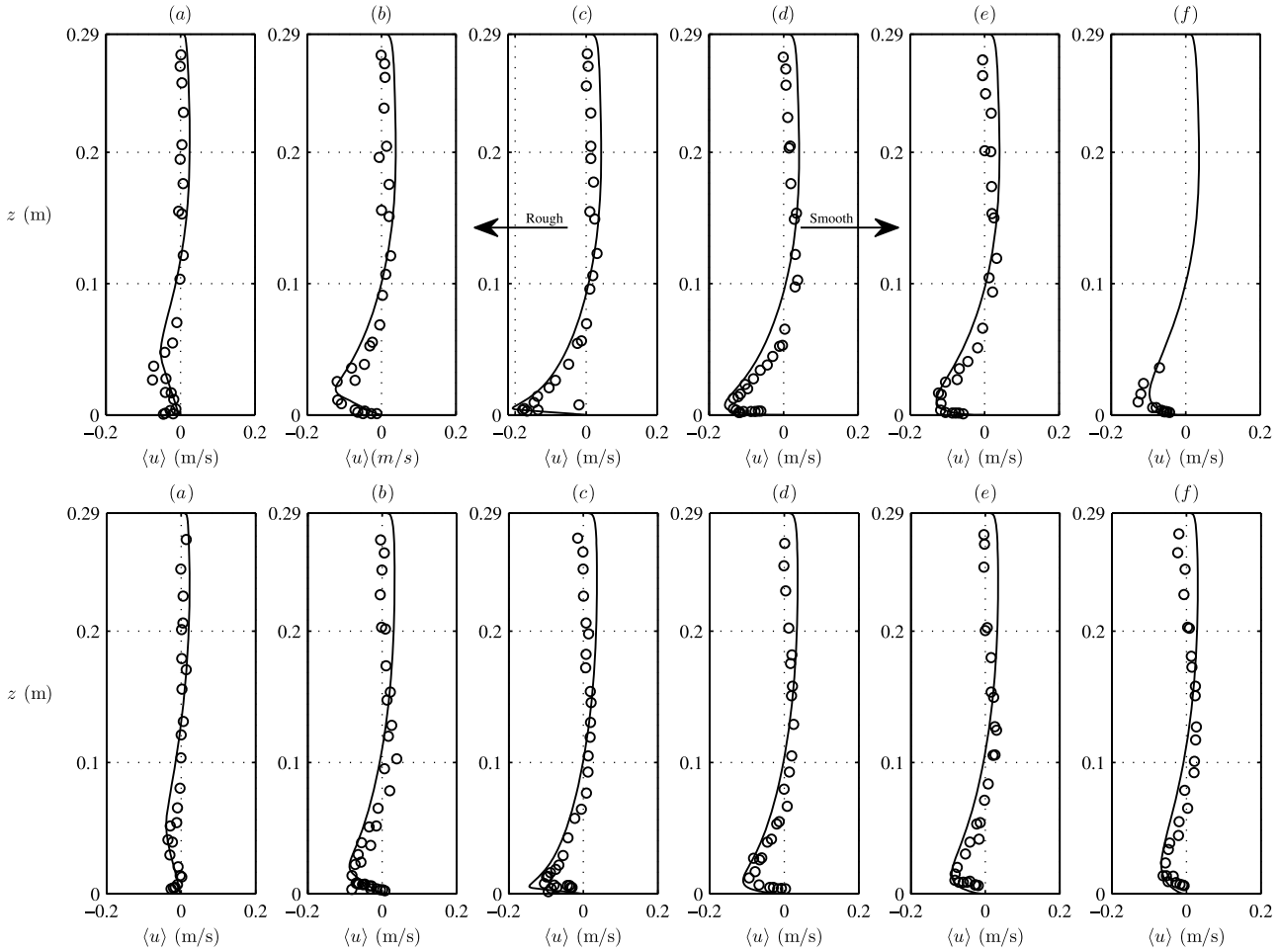

Figure 5. Comparison of computed (full lines) and measured (circles) horizontal period-averaged streaming velocity profiles for (top) Test 1 and (bottom) Test 3 conditions at (a) $x = -80$ cm, (b) −20 cm, (c) −2.5 cm, (d) 10 cm, (e) 20 cm, and (f) 40 cm.

[19] Notice that these are merely generalizations of the previously-stated (leading-order) uniform flow relations (9)–(11).

[20] The comparison of measured and computed profiles for u'_{rms} is made in Figure 6 for the Test 1 conditions. Comparisons are made at a number of x-positions (as in Figure 5) for a phase corresponding to both the maximum ($\omega t = 90°$ (Figure 6, top)) and minimum ($\omega t = 270°$ (Figure 6, bottom)) free stream velocity. A reasonable agreement between computed and measured values is seen at all locations for both phases, generally confirming the ability of the present model to accurately predict turbulence characteristics for the physical problem considered. It can be noted, however, that the model seems to under-predict the production of near-bed turbulence over the hydraulically smooth section (Figures 6d–6f, bottom). This is consistent with known behavior of the k-ω model for steady flows on hydraulically smooth beds [see, e.g., *Wilcox*, 2006, Figures 4.28 and 4.29; *Fuhrman et al.*, 2010, Figure 2c].

[21] Perhaps most notably, both measured and computed results demonstrate asymmetric turbulence properties within the two half-cycles, depending on the direction of the flow. When the flow is positive ($\omega t = 90°$), the results demonstrate markedly higher turbulence levels over the smooth section than when the flow is negative ($\omega t = 270°$). This is due to increased turbulence being advected from the rough section to the smooth section. Additionally, when the flow is negative the elevated turbulence levels over the (left-hand) rough section near the transition are confined closer to the bed than when the flow is positive, as the increased turbulence levels over the rougher section have not yet had as much time to become vertically diffused. Also noteworthy is the computed significantly elevated near-bed turbulence just to the left of the roughness transition (Figure 6c, bottom) when the flow is negative ($\omega t = 270°$). This particular behavior is not directly confirmed (or contradicted) by the measurements, which were not taken sufficiently close to the bed. This increase is, however, consistent with physical expectations, as the high-speed near-bed flow coming off the smooth section will result in increased shear stresses at this location (discussed in more detail in the next subsection), which should in turn be expected to result in an increased production of turbulence in this region. The observed increase in measured turbulence levels away from the bed going from Figure 6c to 6b, would seem consistent with the computed results, as the increased turbulence generated near the bed at the transition is simultaneously

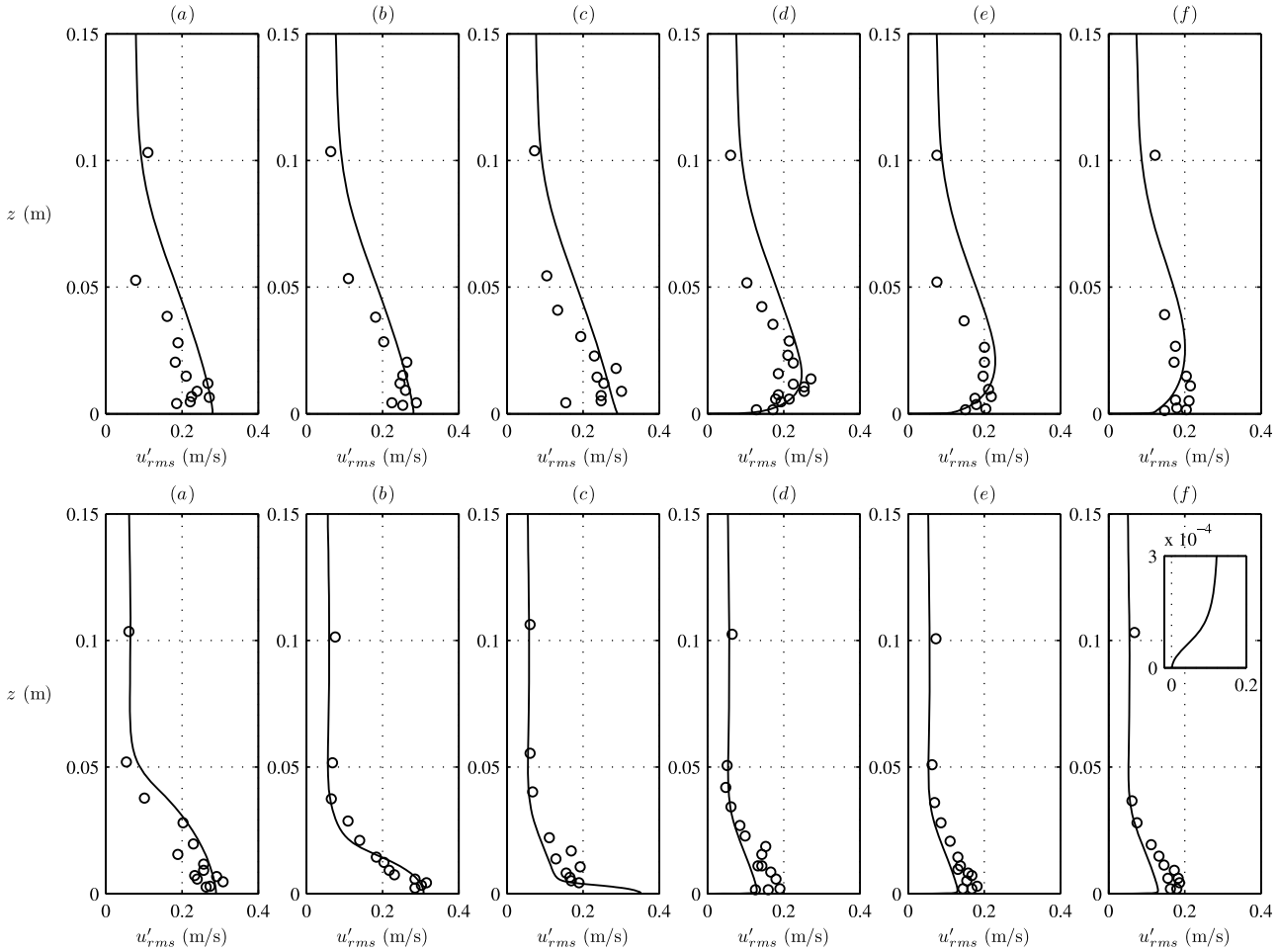

Figure 6. Computed (full lines) and measured (circles) values for the (ensemble averaged) root-mean-squared horizontal fluctuating velocity $u'_{rms} = \sqrt{\overline{u'^2}}$ for Test 1 at (top) $\omega t = 90°$ and (bottom) $\omega t = 270°$ at (a) $x = -80$ cm, (b) -20 cm, (c) -2.5 cm, (d) 10 cm, (e) 20 cm, and (f) 40 cm. The inset in Figure 6f (bottom) depicts a zoomed-in portion of the profile very near the smooth bed.

advected leftward and diffused vertically within the near-bed profile.

[22] At the bed there are also clear differences in the model behavior over the rough (left) and smooth (right) sections that can be seen in Figure 6, which are worth discussing. The imposed $\partial k/\partial z = 0$ boundary condition allows finite values for the turbulent kinetic energy (and hence eddy viscosity ν_T) at the rough wall, whereas the computed results tend to $k = 0$ at the smooth wall. To illustrate the latter behavior more clearly, an inset showing a zoomed-in portion of the computed profile on the smooth bed section is provided in the upper right corner of Figure 6f (bottom). Hence, the model maintains physical consistency over both hydraulically rough and smooth walls, in the sense that a fictitious viscous sublayer is avoided at rough wall sections, whereas a viscous sublayer develops naturally above smooth wall sections. This behavior is in line with the previous demonstration by *Fuhrman et al.* [2010] for steady flows, and confirms similar behavior for unsteady flows.

3.4. Bed Shear Stresses

[23] As a final means of model validation, comparison will be made against the experimental measurements by *Fredsøe et al.* [1993] for measured bed shear stresses. *Fredsøe et al.* [1993] provide spatial variations of measured bed shear stresses (reported as friction velocities) at a number of phases ωt, for both their Test 1 and Test 3 conditions. Additionally, their results were used to provide plots showing the spatial variation of bed shear stress amplification due to the roughness changes, relative to far field values. The present sub-section will include comparisons made in both manners.

[24] Computed and measured spatial variations of the friction velocity U_f are provided in Figure 7 (Test 1) and Figure 8 (Test 3) for a number of phases ωt. Figures 7 and 8 are organized such that Figures 7a and 8a and Figures 7b and 8b, respectively, represent positively- and negatively-directed free stream flow. As seen in both Figures 7 and 8, when the free stream flow is positive (Figures 7a and 8a) i.e. flowing from the rougher (pebble) to the smoother (either smooth or sand paper) section, the friction velocities (and hence bed shear stresses) encountered on either section are very nearly constant, and approximately equal to their far field values. Note that the far field values may be taken as the expected values for each roughness region in the absence of a roughness transition. Alternatively, when the free

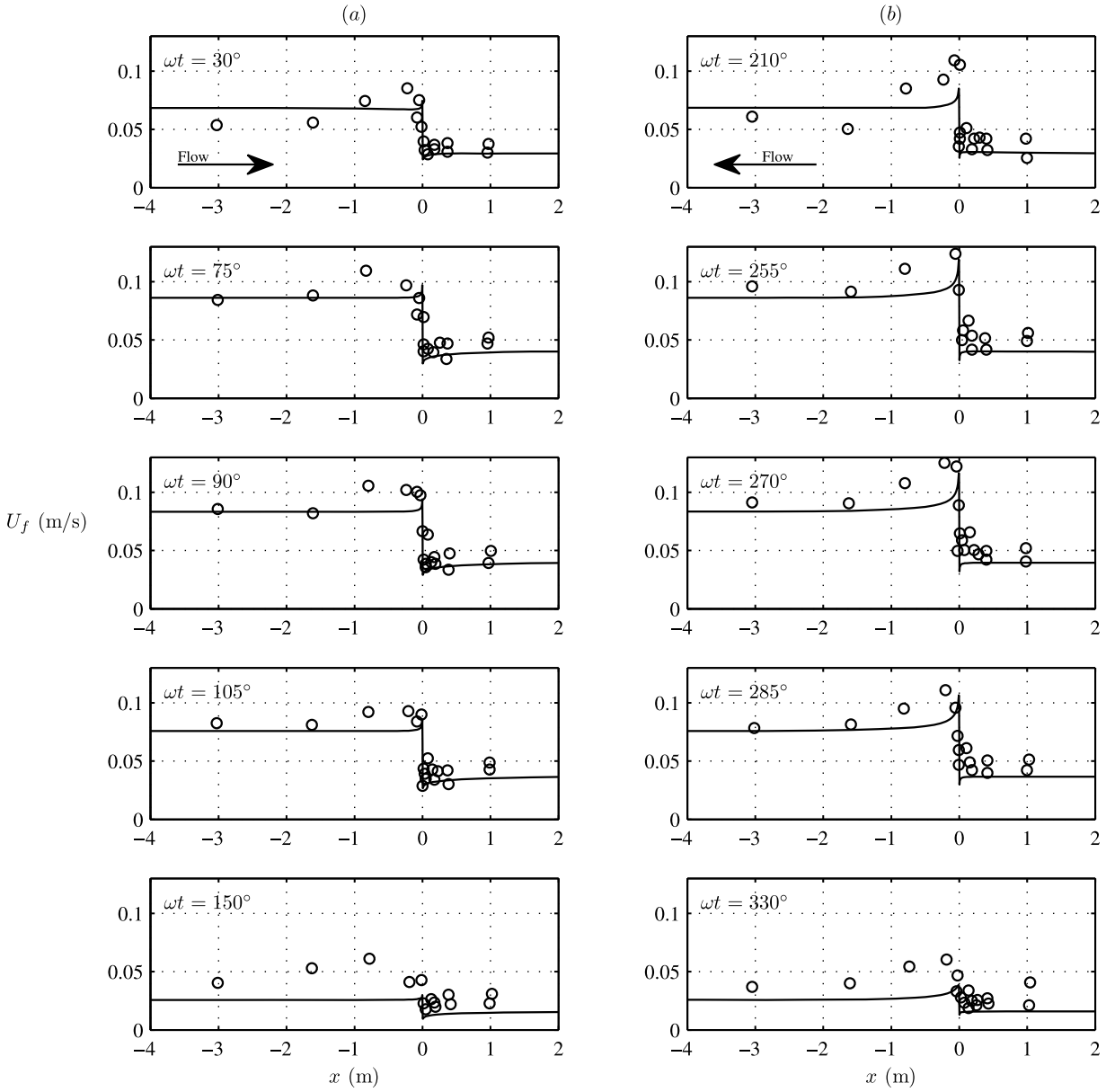

Figure 7. Comparison of computed (full lines) and measured (circles) friction velocity U_f at various phases for Test 1.

stream flow is negative (Figures 7b and 8b) i.e. flowing from the smoother to the rougher section, the friction velocity (and hence bed shear stress) becomes significantly amplified over the rougher (pebble) section, relative to the computed/measured far field values. The reason for the amplification is due to the previously discussed high-speed near-bed flow coming off the smoother section suddenly encountering the added resistance from the larger roughness. The computed variation of the friction velocity for the Test 3 (pebble-to-sand paper transition) conditions are quite good, and appear to match the measured variation somewhat better than the Test 1 (pebble-to-smooth transition) conditions. The model results for Test 1 generally predict a more local amplification than was measured, while also slightly underestimating the peak of the amplification.

[25] This finding is similarly depicted in Figure 9, which shows the spatial variation of the maximum bed shear stress amplification, defined according to

$$\alpha = \frac{\max\left\{U_f^2\right\}}{U_{fm}^2} = \frac{\max\{\tau_b\}}{\tau_{bm}}, \tag{24}$$

where τ_{bm} is the maximum value of the undisturbed (far field) bed shear stress over the pebble section and $\max\{\tau_b\}$ is the maximum value of the bed shear stress achieved at a given position over the rougher section. Hence α represents the amplification factor of the bed shear stress over the rougher section due to the bottom roughness transition. The resulting amplifications experienced for both Test 1 and Test 3 are presented in Figure 9, both of which illustrate a

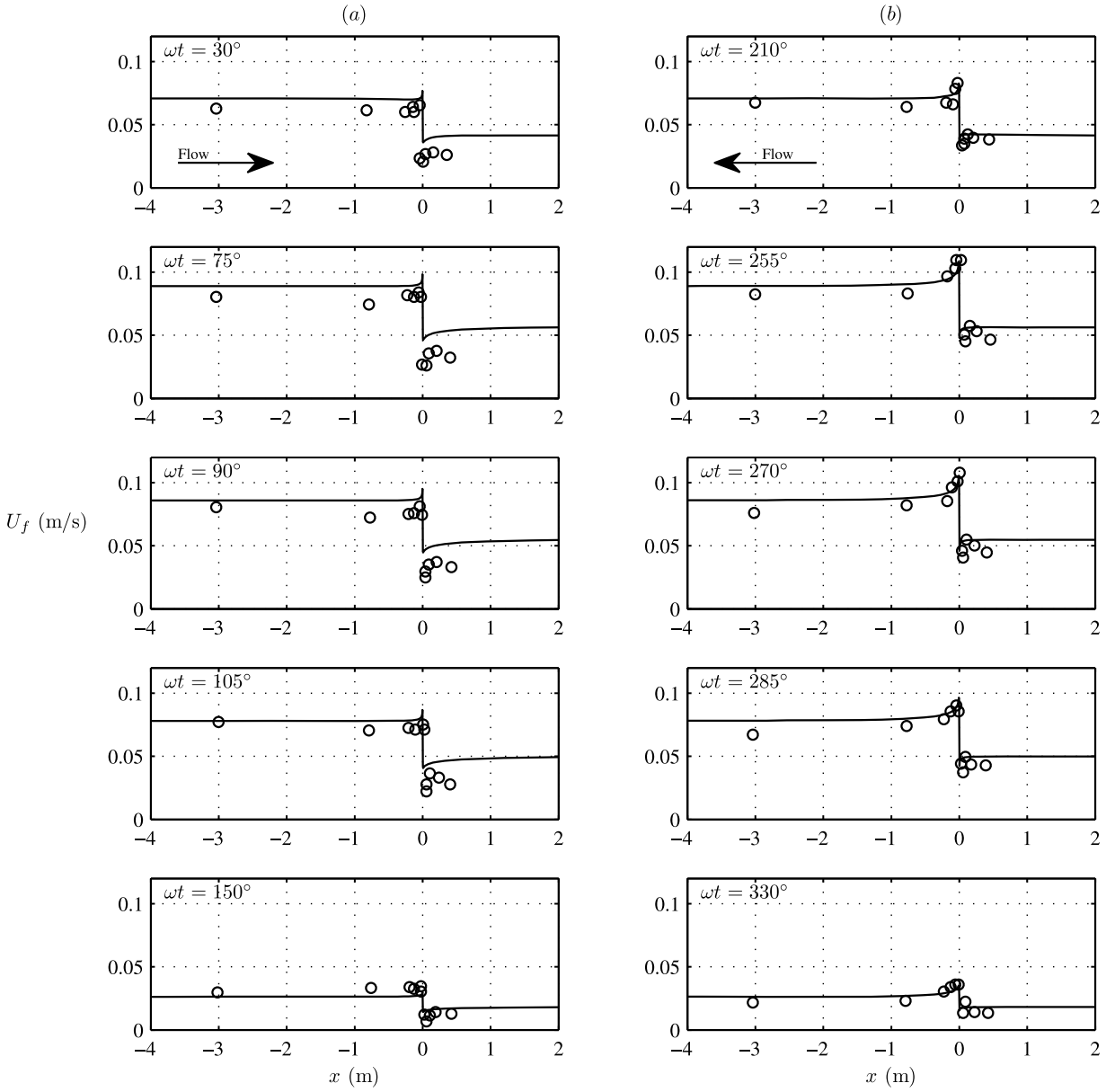

Figure 8. Comparison of computed (full lines) and measured (circles) friction velocity U_f at various phases for Test 3.

significant amplification of the bed shear stress in the immediate vicinity of the roughness change. When comparing the results for Test 1 (Figure 9a), the maximum value of α is slightly under-predicted ($\alpha_{max} = 2.2$ versus measured 2.5), while the amplification in the model is again confined to a region closer to the roughness change than in the experimental measurements, as mentioned above. These discrepancies are likely related to the under-prediction of turbulence generated on the hydraulically smooth bed, as mentioned previously in the discussion of Figures 6d–6f (bottom). The results for Test 3 (Figure 9b), where both sections are hydraulically rough, are in good agreement, both in terms of the maximum amplification as well its spatial variation.

[26] This concludes the validation of the model against the experimental measurements by *Fredsøe et al.* [1993] involving oscillatory boundary layer flow over a step change in the bottom roughness. Based on our comparisons, the present model provides reasonable results regarding the period-averaged horizontal velocity profiles, turbulence quantities, as well as bed shear stresses (and their amplification) in the vicinity of the roughness change. The results are particularly accurate when both sides are hydraulically rough, which is the situation likely to be of most practical importance, and the focus of the parametric study that follows.

4. Normally-Directed Oscillatory Flow ($\theta = 0°$)

[27] This section will extend the previous results based on the isolated experimental conditions of *Fredsøe et al.* [1993], i.e. we will now use the model to conduct a sys-

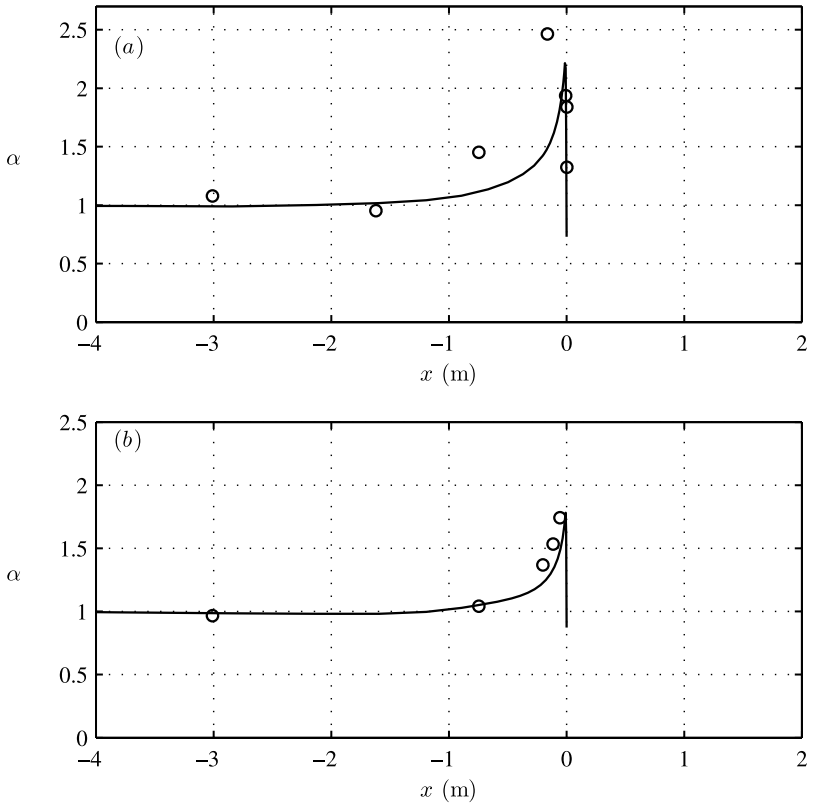

Figure 9. Comparison of computed (full lines) and measured (circles) spatial variation of the bed shear stress amplification α for (a) Test 1 and (b) Test 3.

tematic parametric study for the physical problem at hand. More specifically, we aim to monitor both the bed shear stress (and its amplification) and period-averaged streaming characteristics (the quantities of most practical importance), subject to systematic variation of the important non-dimensional parameters governing the oscillatory flow on spatially varying bottom roughness. In all forthcoming simulations, care has been taken to ensure that $k'_N U_{fm}/\nu \geq 70$ is satisfied over the less-rough section, hence all results fall within the hydraulically rough regime. The present section will be limited to cases with $\theta = 0°$ i.e. oscillatory flow directed normal to the transitional roughness (see again Figure 1). Both sudden and gradual roughness transitions will be considered.

4.1. Sudden Roughness Transitions

[28] On dimensional grounds, it can be surmised that the problem of oscillatory flow over a sudden change in bottom roughness, assuming fully rough turbulent conditions (i.e. no Reynolds number dependence) and fixed flow direction $\theta = 0°$, can be characterized by two dimensionless quantities, which for the purposes of the present study have been selected as

$$\frac{a}{k_N}, \qquad \frac{k_N}{k'_N}, \tag{25}$$

where $a = U_{1m}/\omega$ is again the amplitude of free-stream orbital motion. In what follows, both the bed shear stress (including its amplification) and the induced streaming will be studied based on systematic variation of these two non-dimensional quantities. For our parametric study, we will consider variable roughness ratios $1 \leq k_N/k'_N \leq 100$ over the range $20 \leq a/k_N \leq 500$, representing realistic combinations likely to be encountered in practice e.g. if the larger roughness k_N is taken to represent a stone protection layer, with the smaller roughness k'_N representing underlying natural sediment. Based on comparison of wave friction factors against experimental measurements, *Fuhrman et al.* [2009a] have previously demonstrated acceptable accuracy for the k-ω model for $a/k_N \geq 20$.

[29] Whereas the previous simulations in section 3 used friction walls at both top and bottom boundaries, to match the experimental conditions of *Fredsøe et al.* [1993], the present parametric study will alternatively make use of a simpler setup, with a frictionless rigid lid as the top boundary. Hence, only a single boundary layer is created and resolved near the bottom wall, as this is the location of principal interest. Accordingly, rather than using a four-block structure as shown in Figure 3, the present results make use of an otherwise similar model domain consisting of only the bottom two blocks, each having fixed width $b/a = 3$. Note also that while the previously considered experimental conditions correspond to $D/a \approx 0.05$, the present results will use a larger model domain height D fixed such that $D/a = 1$. As the oscillatory wave boundary layer thickness δ on rough beds typically corresponds to $\delta/a =$

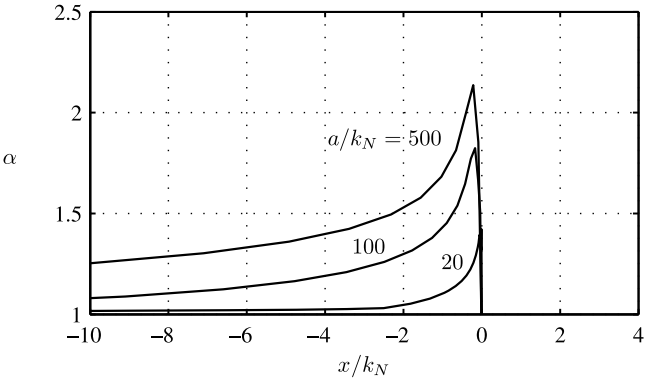

Figure 10. Examples demonstrating the spatial variation of the maximum phase-resolved bed shear stress amplification α versus x/k_N for a/k_N = 500, 100, and 20, all with fixed k_N/k'_N = 100, and θ = 0°.

0.03–0.05 for the range of parameters considered, e.g. based on *Fredsøe and Deigaard* [1992, (2.45)]:

$$\frac{\delta}{a} = 0.09\left(\frac{a}{k_N}\right)^{-0.18}, \tag{26}$$

this condition ensures that the wave boundary layer thickness is at least an order of magnitude smaller than the total height of the computational domain.

[30] To illustrate the computed results, three examples showing the computed spatial variation of the bed shear stress amplification α are first depicted in Figure 10, for a/k_N = 500, 100, and 20, all with fixed k_N/k'_N = 100 i.e. the largest roughness ratio considered. Consistent with the previous simulations, these results demonstrate potentially significantly amplified bed shear stresses as a result of a sudden roughness transition. As seen, regardless of a/k_N, the largest amplification of the bed shear stress is confined to relatively small distances from the transition of the order of the roughness length k_N. The amplification generally increases with a/k_N, with a maximum computed value of $\alpha_{\max}$ = 2.14 predicted for a/k_N = 500. This value seems consistent with expectations from earlier steady flow considerations of *Belcher et al.* [1990], who found $\alpha_{\max}$ = 2.5, for a case having k_N/k'_N = 125. The lesser, but comparable, value predicted here for oscillatory flows seems consistent with physical expectations, as oscillatory boundary layer characteristics should in principle approach steady current behavior at the limit $a/k_N = \infty$. That $\alpha_{\max}$ decreases with decreasing a/k_N also makes physical sense, considering e.g. that (for fixed k_N, k'_N, and T) reductions in this parameter correspond to reductions in the flow velocity U_{1m}.

[31] Computed results for the bed shear stress over the full parametric range considered are summarized in Figure 11. These are presented in two ways. Figure 11a presents results in terms of a generalized wave friction factor, defined according to

$$f_w = \frac{2\max\{\tau_b\}}{\rho U_{1m}^2}. \tag{27}$$

Notice that for the special case where there is no roughness change (k_N/k'_N = 1) then f_w defaults to its standard (uniform roughness) definition originally introduced by *Lundgren and Jonsson* [1961]. Additionally, the results are presented in terms of the bed shear stress amplification in Figure 11b, where $\alpha_{\max}$ is again the largest amplification experienced over the entirety of the rougher section. For small roughness ratio k_N/k'_N the results for the bed shear stress amplification for various a/k_N do not vary too significantly, whereas these differences become more pronounced for say $kN/k'_N \geq 10$.

[32] A similar parametric study has in fact been considered previously by *Laursen et al.* [1994] using a one-dimensional Lagrangian approach, in conjunction with the k-ε turbulence model of *Justesen* [1988]. Direct comparison with the present Figure 11 can be made with their Figure 9. While qualitatively similar, the earlier results of *Laursen et al.* [1994] generally suggest larger bed shear stress amplifications than found in the present study, with a much greater sensitivity with respect to the parameter a/k_N. Specifically, *Laursen et al.* [1994] found values for $\alpha_{\max}$ of up to 3.5, even though most of their presented curves for a given a/k_N did not span the full range to k_N/k'_N = 100 (i.e. extrapolation of these curves would suggest yet larger values). These discrepancies are apparently due to the

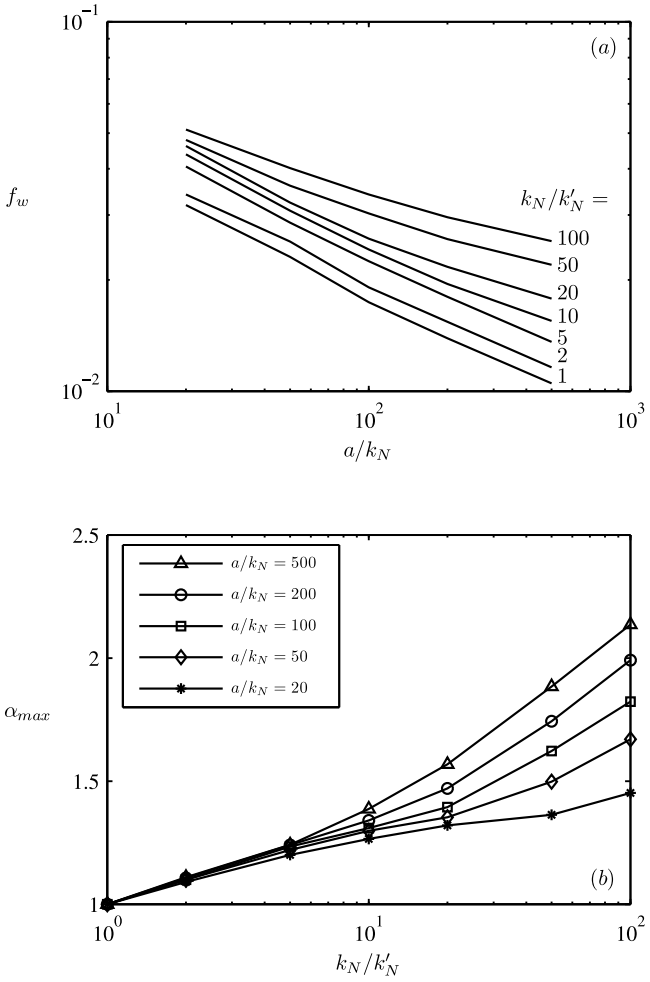

Figure 11. Computed summary of the (a) wave friction factor f_w and (b) maximum bed shear stress amplification $\alpha_{\max}$ for oscillatory flow simulations involving sudden roughness changes, with θ = 0°.

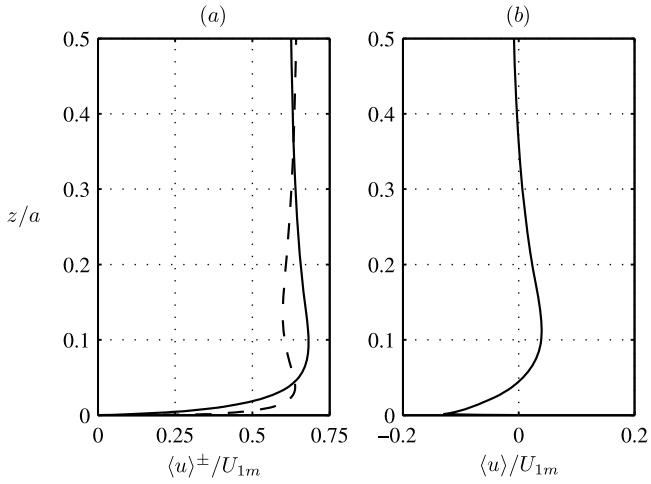

Figure 12. Computed horizontal velocity profiles at $x = 0$ for $a/k_N = 20$, $k_N/k'_N = 100$, and $\theta = 0°$ averaged over (a) positive $\langle u\rangle^+$ (full line) and negative $\langle u\rangle^-$ (dashed line) half-periods, and (b) the full period. Note that in Figure 12a the profile for the negative half-period (dashed line) is shown as positive, to ease comparison between the successive half-periods.

difference between their one-dimensional Lagrangian description with the present two-dimensional description, as well as to differences in the turbulence models utilized. Given that the physical problem considered is in fact two-dimensional in nature, the present results are expected to be more accurate, and Figure 11 is therefore presented as an improved diagram for predicting bed shear stresses and their amplification for wave boundary layer problems involving sudden bottom roughness transitions. In support of this contention, we mention that the present (unconfined) results with $k_N/k'_N = 20$, $a/k_N = 200$ give $\alpha_{\max} = 1.5$, which remains in reasonable agreement with the experimentally measured value $\alpha_{\max} = 1.7$ of *Fredsøe et al.* [1993], having similar parameters (Test 3, with $k_N/k'_N = 17.9$, $a/k_N = 210$; see Figure 9b). This is in contrast to the significantly larger $\alpha_{\max} = 3.2$, estimated from *Laursen et al.* [1994, Figure 9], for the same parameters.

[33] Results from the parametric study for the maximum (in magnitude) period-averaged horizontal streaming velocity u_s over the entirety of the model domain will also be presented. As an example, the computed period-averaged velocity profiles $\langle u\rangle/U_{1m}$ at $x = 0$ for the specific case with $a/k_N = 20$ and $k_N/k'_N = 100$, which in fact corresponds to the case giving the largest streaming velocity for the range of parameters considered, is first provided in Figure 12. The horizontal profiles are presented averaged over both half- (Figure 12a) and full-periods (Figure 12b), in a fashion analogous to the previously presented Figure 4. As expected, the results from the present parametric study show near-bed period-averaged streaming velocities in the direction of larger roughness, again due to the larger near-bed velocity gradients experienced when the flow is directed towards the larger roughness section. Additionally, period-averaged flow in the opposite direction is observed further up in the profile. This is caused by so-called overshooting of the velocity profile within the boundary layer, which occurs higher up in the column when the flow is positively directed, as boundary layer thickness increases with roughness. In contrast to the confined results (based on the laboratory experiments, Figures 4 and 5), the present configuration allows the streaming profile to essentially asymptotically approach zero for large distances above the boundary layer, as seen in Figure 12b. Also shown in Figure 13 are contour plots depicting the spatial distribution of the period-averaged horizontal velocities $\langle u\rangle$ for both $a/k_N = 500$ (Figure 13a) and $a/k_N = 20$ (Figure 13b), again with $k_N/k'_N = 100$. This illustrates that the induced streaming is most intense in the immediate vicinity of the roughness change, and that its horizontal extent can range from $O(10k_N)$ to $O(100k_N)$, depending on the value of a/k_N, i.e. this extent scales approximately with a.

[34] The results for the maximum period-averaged streaming velocity for the full parametric range tested are summarized in Figure 14. Consistent with the findings of [*Fredsøe et al.*, 1993] and section 3, the present parametric study suggests near-bed period-averaged streaming velocities of the order $u_s/U_{1m} = O(-0.1)$, where the negative sign again indicates flow towards the larger roughness. From

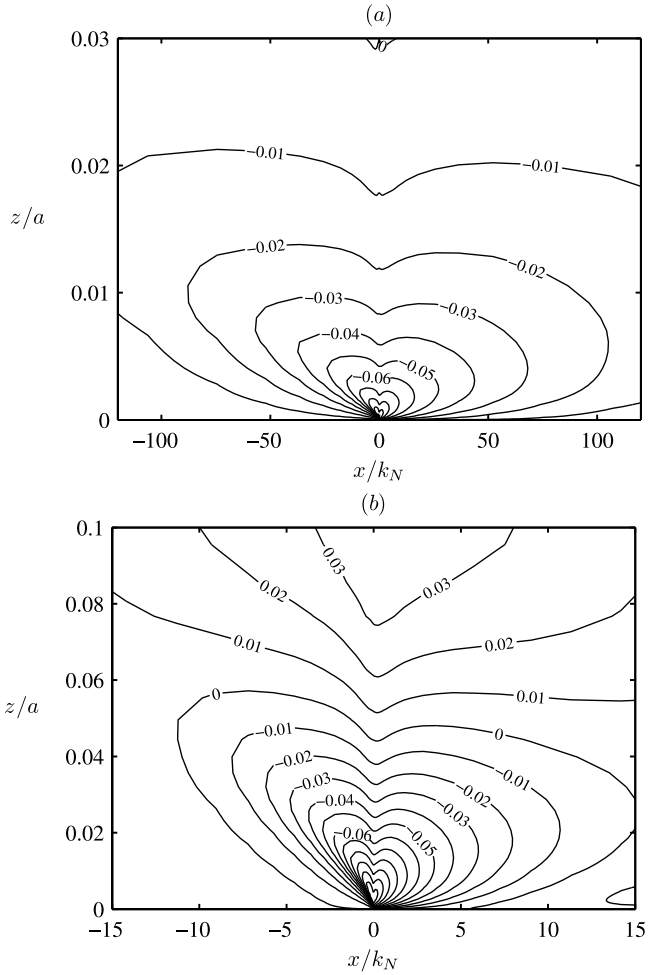

Figure 13. Contour plot of computed period-averaged horizontal velocities $\langle u\rangle/U_{1m}$ for sudden roughness transitions with fixed $k_N/k'_N = 100$, $\theta = 0°$, and (a) $a/k_N = 500$ and (b) $a/k_N = 20$.

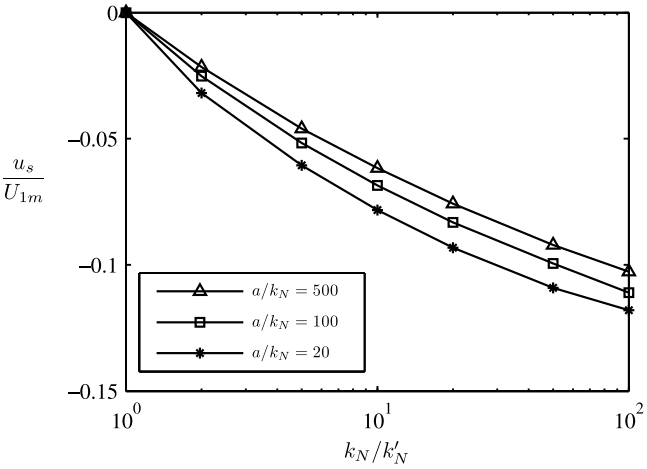

Figure 14. Summary of largest computed period-averaged streaming velocities for oscillatory flows with a sudden change in bottom roughness, with $\theta = 0°$.

Figure 14 it is seen that the model predicts only rather weak dependence of the results on the parameter a/k_N. As such, only curves corresponding to three values of a/k_N are shown, though intermediate values have also been tested, in accordance with the previously depicted results in Figure 11. Consistent with the findings previously discussed in conjunction with Figure 11, the presently found dependence of the streaming on a/k_N is much weaker than depicted in the earlier one-dimensional results of *Laursen et al.* [1994]. For the above mentioned reasons, we again expect the present results to be more accurate, as the problem is now properly resolved in two spatial directions. The slight increase in the magnitude of u_s/U_{1m} for decreasing a/k_N is also consistent with physical expectations, in the sense that the non-dimensional streaming grows with increasing non-dimensional roughness.

4.2. Gradual Roughness Transitions

[35] The previous results involving a sudden (step) change in bottom roughness will now be complemented by considering the related effects of a gradual roughness transition under otherwise similar oscillatory flow conditions. To the authors' knowledge, such effects have not been previously studied in detail. This situation may be taken to loosely represent a wave boundary layer e.g. at locations where natural (or otherwise) sediment grading has occurred. The gradual roughness change is implemented by defining a region having a linear transition in bottom roughness (i.e. from k_N to k'_N) over a horizontal distance λ. Taking the center of this region as the origin, this change therefore occurs over $-\lambda/2 \le x \le \lambda/2$, as illustrated in Figure 15.

[36] In terms of the parametrization, the introduction of this feature necessitates an additional non-dimensional parameter. Hence, the two-dimensional space considered previously (25) now becomes three-dimensional, consisting e.g. of:

$$\frac{a}{k_N}, \qquad \frac{k_N}{k'_N}, \qquad \frac{\lambda}{k_N}. \tag{28}$$

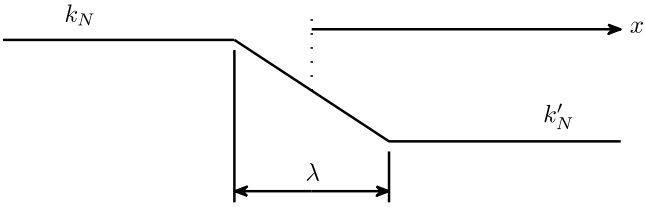

Figure 15. Definition sketch illustrating a gradual (linear) change in bottom roughness over distance λ.

The previously considered step changes in roughness now correspond to special cases with $\lambda/k_N = 0$. To avoid spanning the full, three-dimensional, parametric space we will fix $k_N/k'_N = 100$ in what follows. This corresponds to the maximum roughness ratio considered in section 4.1, hence using this value will lead to the most pronounced effects for a given combination of a/k_N and λ/k_N over the parametric range considered. Both the effects on the bed shear stress amplification and horizontal streaming velocity will again specifically be monitored.

[37] Examples depicting the spatial distribution of the bed shear stress amplification α are depicted in Figure 16, for cases with $\lambda/k_N = 0$, 0.5, and 5, with fixed $a/k_N = 500$. As can be seen, the special case with $\lambda/k_N = 0$ (i.e. a sudden roughness change) is identical to that shown previously in Figure 10. From Figure 16 it is seen that gradually varying bottom roughness can significantly reduce the bed shear stress amplification. As the sharp peak in α for $\lambda/k_N = 0$ occurs very locally in space, as previously discussed, it becomes effectively eliminated when a roughness change is imposed gradually, even over relatively short distances the order of the roughness length k_N.

[38] This is further illustrated in Figure 17, which shows the summary of computed maximum bed shear stress amplification $\alpha_{\max}$ versus λ/k_N for three values of $a/k_N = 20$, 100, and 500. As can be seen, the resulting amplification of the bed shear stress is significantly reduced for say $\lambda/k_N \ge 10$, regardless of a/k_N. As λ/k_N becomes small, the results expectedly approach those from the previous section with $\lambda/k_N = 0$. The results with $\lambda/k_N = 0$ (Figure 11) can therefore obviously be considered conservative. For flows over naturally sorted sediments, or wherever a roughness transition is expected to be gradual, the present results suggest that the

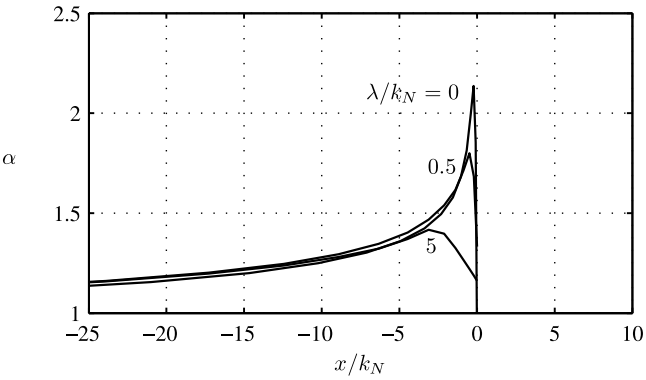

Figure 16. Examples demonstrating the spatial variation of the maximum bed shear stress amplification α for $a/k_N = 500$, $k_N/k'_N = 100$, and $\theta = 0°$, with $\lambda/k_N = 0$, 0.5, and 5.

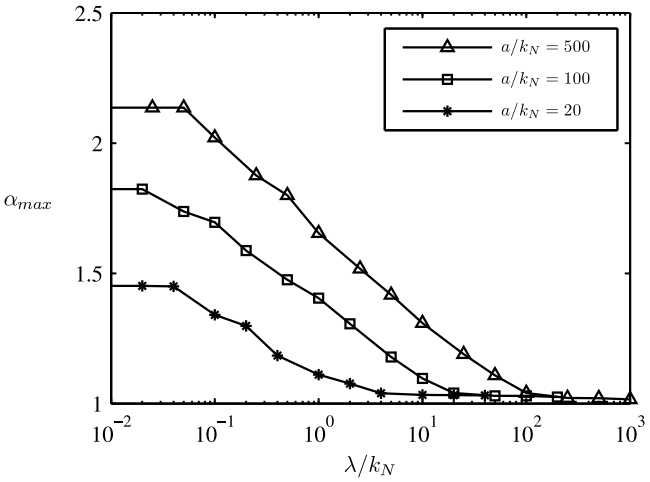

Figure 17. Summary of maximum computed bed shear stress amplifications over beds having a gradual (linear) change in roughness (using fixed $k_N/k'_N = 100$ and $\theta = 0°$) over the distance λ.

experienced bed shear stress amplifications may be much less than indicated in Figure 11, however.

[39] The summary for the maximum computed period-averaged streaming velocity u_s is similarly shown in Figure 18. It is again emphasized that the presented negative streaming values correspond to near-bed streaming in the direction of larger roughness. Consistent with the previous results depicted in Figure 14, the computed streaming velocities are again not particularly sensitive to changes in the parameter a/k_N. Interestingly, these streaming results are also much less sensitive to the effects of gradual roughness change than are those of the just-discussed bed shear stress amplification. For example, for $\lambda/k_N \leq 1$ the results are almost the same as for $\lambda/k_N = 0$, whereas even for $\lambda/k_N \approx 10$ the computed streaming is still typically of the same order of magnitude i.e. $u_s/U_{1m} = O(-0.1)$, regardless of a/k_N.

[40] Insight regarding this lack of sensitivity can be gained by inspection of the spatial distribution of the period-averaged horizontal velocities. As an example, Figure 19 depicts a contour plot for the period-averaged horizontal velocities $\langle u \rangle$ corresponding to a case with $a/k_N = 20$, $k_N/k'_N = 100$, and $\lambda/k_N = 10$. Note that this plot is directly comparable with Figure 13b, having identical a/k_N and k_N/k'_N, but with $\lambda/k_N = 0$. As expected from Figure 18, the streaming in the case having gradual roughness change (Figure 19) is indeed less, but of comparable magnitude, as for the case with a sudden change (Figure 13). Interestingly, it is seen that the location of maximum streaming in Figure 19 is shifted rightwards (i.e. to the less-rough side of the transitional patch, $x \approx \lambda/2$) when compared to Figure 13 where it is centered around $x = 0$. This phenomenon can be explained by considering what happens over the positive and negative half-cycles of the oscillatory flow. When the flow is directed leftward (i.e. towards increasing roughness) it adjusts much more rapidly in space than when the flow is directed rightward (i.e. towards decreasing roughness). Therefore, the velocity profiles during the positive half-cycle will somewhat resemble those of the rougher section over the entirety of the transitional patch. Alternatively, the profiles averaged over the negative half-cycle will only resemble those for the smaller roughness at the right-hand side of the transition patch. Hence, the differences in the two half-cycles will be most pronounced near the smoother side of the spatial transition, explaining the rightward shift in the location of maximum streaming observed in Figure 19. Consistent with this explanation, the period-averaged values at this particular location will be less than, but still comparable in magnitude, to those for a sudden roughness transition. Hence, these considerations also explain how the streaming over gradual roughness transitions can maintain significant strength, even in situations where the bed shear stress amplification is significantly reduced.

[41] The observed spatial shift in streaming towards smaller roughness may have practical implications. For example, it may limit the extent to which suspended natural sands could spread over a stone protection layer.

5. Arbitrarily-Directed Oscillatory Flow ($0° \leq \theta \leq 90°$)

[42] All of the preceding results have considered oscillatory flows directly normal to the line (or plane) of bottom roughness transition, i.e. with $\theta = 0°$. This section will extend the former findings by considering the effects of variable flow orientation in plan, as again depicted conceptually in Figure 1. To the authors' knowledge, these effects have not been previously studied within oscillatory flows, either experimentally or numerically.

[43] With the introduction of an arbitrary flow direction θ, the dimensionless parameter space (28) now becomes four-dimensional, consisting e.g. of:

$$\frac{a}{k_N}, \qquad \frac{k_N}{k'_N}, \qquad \frac{\lambda}{k_N}, \qquad \theta. \tag{29}$$

In what follows we will again fix the roughness ratio to be large $k_N/k'_N = 100$ and only consider sudden roughness transitions $\lambda/k_N = 0$, in order to isolate the present effects from those considered previously. As before we will con-

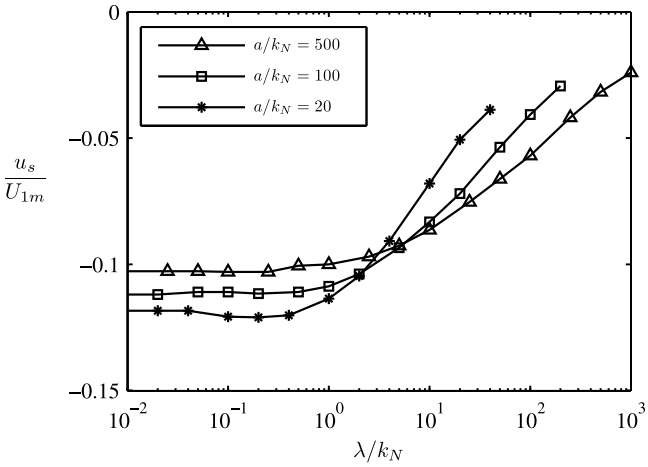

Figure 18. Summary of largest computed period-averaged streaming velocities for simulations involving gradual (linear) changes in bottom roughness, with fixed $k_N/k'_N = 100$ and $\theta = 0°$.

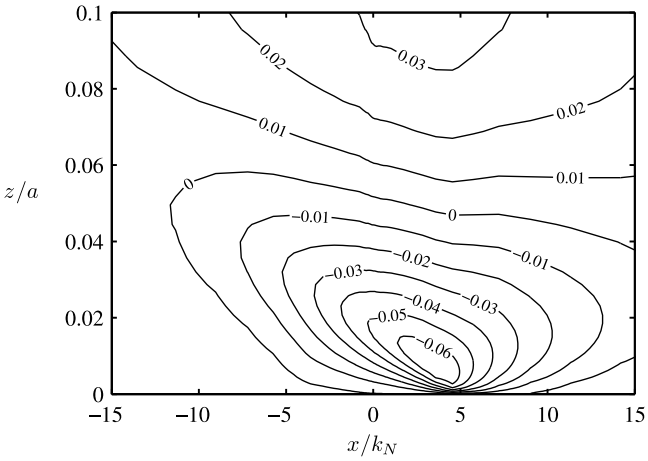

Figure 19. Contour plot of computed period-averaged horizontal velocities $\langle u\rangle/U_{1m}$ ($a/k_N = 20$, $k_N/k'_N = 100$, $\theta = 0°$) over a gradual change in roughness ($\lambda/k_N = 10$).

sider three values of the ratio $a/k_N = 500$, 100, and 20. The flow direction will be varied over its full unique range $0° \le \theta \le 90°$. Specific attention will here be paid to the induced period-averaged streaming characteristics in the x-direction i.e. normal to the line of transitional roughness.

5.1. In-Line Oscillatory Flow ($\theta = 90°$)

[44] We will begin by considering special cases at the limit $\theta = 90°$ i.e. oscillatory flow in-line with, rather than normal to, the transitional roughness (see again Figure 1). As examples, two contour plots (for $a/k_N = 500$ and 20, respectively) depicting the spatial distribution of the computed period-averaged horizontal velocities $\langle u\rangle/U_{1m}$ are provided in Figure 20. Most interestingly, from these plots it is seen that with $\theta = 90°$, the computed period-averaged flow normal to the transitional roughness $\langle u\rangle$ is not zero, but has instead shifted in sign from that discussed previously, i.e. it is now positive, implying flow directed towards the lower roughness. As the dominant oscillatory flow at this limit is forced in the pure y-direction, these plots therefore demonstrate development of secondary transverse flows of the order $\langle u\rangle/U_{1m} = O(0.01)$, with a maximum computed value ≈0.05 i.e. roughly half the magnitude previously found for $\theta = 0°$. These secondary flows remain appreciable for $O(10k_N)$–$O(100k_N)$, depending on the value of a/k_N.

[45] The reason for the predicted secondary flows can be traced to anisotropy in the turbulent normal stresses τ_{xx} and τ_{zz}. This is consistent with the arguments of *Speziale* [1982], who (taking the y-direction as streamwise) identified the importance of

$$\frac{\partial^2(\tau_{xx} - \tau_{zz})}{\partial x \partial z} \tag{30}$$

as an axial vorticity source term, while studying secondary flows within rectangular pipes. The turbulence generated over rougher sections can be much larger than over smoother sections. Hence, large gradients in the turbulent kinetic energy density k can develop in the vicinity of a spatial roughness transition. A turbulence model incorporating anisotropic τ_{xx} and τ_{zz} will in turn result in finite (30), thereby promoting secondary transverse flows, as illustrated e.g. in Figure 20. This is in contrast to a turbulence model predicting isotropic normal stresses, which would invariably predict (30) to be zero, regardless of the variation of k. As a check that this is indeed the cause of the predicted phenomenon, we note that when these simulations are repeated with a standard Boussinesq approximation i.e. taking $a_{(i)} = 2/3$ in (6), these large-scale secondary flows disappear. Hence, a model incorporating anisotropic turbulent normal stresses is essential for the prediction of this phenomenon. This is again achieved in the present work via the alternative use of (8).

5.2. Oblique Oscillatory Flow ($0° \le \theta \le 90°$)

[46] We will now consider more general cases involving oblique oscillatory flow. Based on the previous findings, for oblique oscillatory flows with $0° < \theta < 90°$ we can expect a competition of sorts between two different phenomena. For small θ (flow predominantly normal to the transitional roughness) we can expect negative streaming (i.e. towards larger roughness), due to differences in the x-component of the oscillatory flow over the two half-cycles, as discussed

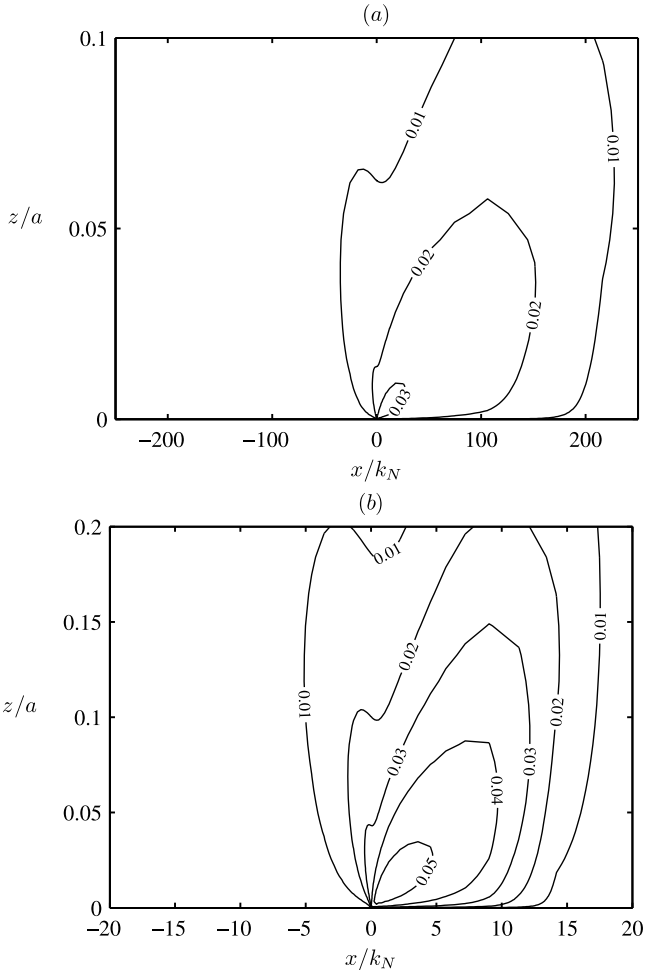

Figure 20. Contour plots of computed period-averaged horizontal velocities $\langle u\rangle/U_{1m}$ for cases involving sudden roughness transitions with fixed $k_N/k'_N = 100$ and $\theta = 90°$, with (a) $a/k_N = 500$ and (b) $a/k_N = 20$. Note the different horizontal and vertical scales on each plot.

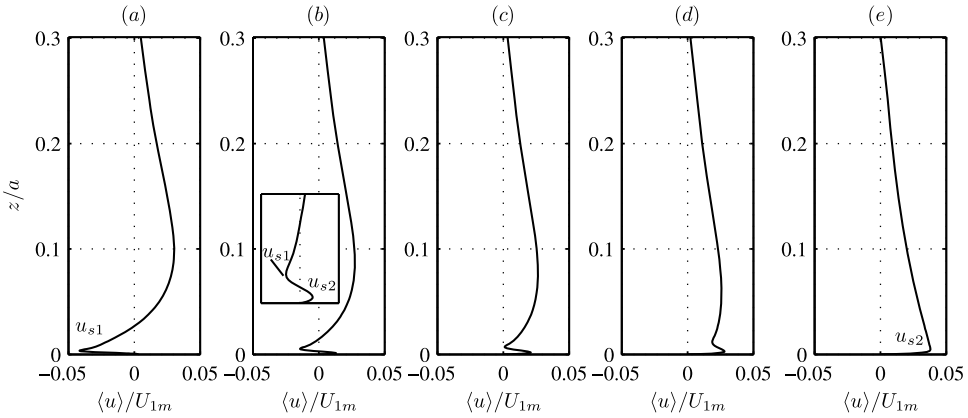

Figure 21. Computed period-averaged velocity $\langle u\rangle/U_{1m}$ profiles at $x = 0$ for $a/k_N = 20$ and $k_N/k'_N = 100$ with oscillatory flow direction (a) $\theta = 60°$, (b) 70°, (c) 75°, (d) 80°, and (e) 90°.

previously in section 3.2 and section 4. Alternatively, for sufficiently large θ (flow predominantly in-line with the transitional roughness), we can expect the secondary flows identified in the previous sub-section to dominate, leading to positive period-averaged flow towards smaller roughness.

[47] These expectations are largely confirmed in Figure 21, which depicts a series of computed period-averaged velocity $\langle u\rangle/U_{1m}$ profiles (with fixed $a/k_N = 20$) at $x = 0$, over the range $60° \le \theta \le 90°$. As seen there, for $\theta = 60°$ (Figure 21a) negative streaming within the boundary layer (approximately $z/a \le 0.05$) occurs, qualitatively similar to that displayed earlier e.g. in Figure 12b with $\theta = 0°$. Upon close inspection of Figure 21a, however, small positive streaming velocities can in fact be detected very near the bed. Interestingly, for slightly larger angles, e.g. $\theta = 70°$ (Figure 21b), the near-bed profile becomes more obviously doubly-peaked, and boundary layer streaming in both positive and negative directions is clearly apparent. This is due to the simultaneous action of the two competing mechanisms. In such cases, for future discussion, we will denote the upper (local minimum) streaming velocity u_{s1}, and the lower (local maximum) streaming velocity u_{s2}, as depicted in the inset of Figure 21b. It is stressed that these local extrema can, but do not necessarily, take opposite signs. As the forced flow direction is further increased e.g. to $\theta = 75°$ (Figure 21c) the positive secondary flows become more dominant, though remnants of the negative boundary layer streaming are still easily identifiable via the local minimum in the profile (in this case both u_{s1} and u_{s2} are positive). These remnants are less noticeable for $\theta = 80°$ (Figure 21d), and disappear altogether at the limit $\theta = 90°$ (Figure 21e), where the mechanism giving rise to the positive secondary flows becomes isolated. At this limit the profile is singly-peaked, and only the local maximum u_{s2} exists.

[48] These characteristic streaming velocities (u_{s1} and u_{s2}) are summarized for variable θ in Figure 22, for the three a/k_N values considered. Unlike the previous depictions, this plot now consists of two distinct families of curves, one each for u_{s1} and u_{s2}. As should be expected, for small θ the streaming is predominantly negative, as indicated by the sole presence of the u_{s1} family of curves for $\theta < 60°$. Alternatively, for large $\theta > 80°$, the positive streaming due to the secondary currents is dominant. In this range no local minima could be detected in the period-averaged profiles, hence only the u_{s2} family of curves exists. Interestingly, for oblique oscillatory flows within the transitional range $60° \le \theta \le 80°$ both curve families exist, indicating doubly-peaked boundary layer streaming profiles, as just illustrated in Figure 21. The sensitivity on the induced streaming properties for various a/k_N is again weak, in line with the findings of earlier sections.

[49] The sediment transport implications within the transitional range $60° \le \theta \le 80°$ are likely rather complicated, and will not be speculated upon here. Those regarding the secondary flows predicted at the $\theta = 90°$ limit are more readily discernable, however, and are discussed further in the following section.

6. Discussion and Prediction of Transverse Circulation Cells

[50] The prediction of transverse roughness-induced secondary currents within oscillatory wave boundary layer flows (e.g. as depicted in Figure 20 for $\theta = 90°$) is new, and may be important within the natural sorting of graded sediments in coastal regions. The larger turbulence gener-

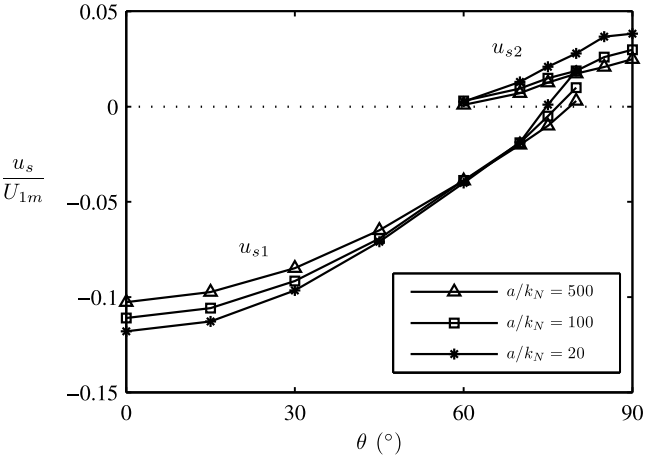

Figure 22. Summary of largest computed period-averaged horizontal boundary layer streaming velocities u_s for simulations involving sudden roughness change ($k_N/k'_N = 100$) with varying oscillatory flow direction θ.

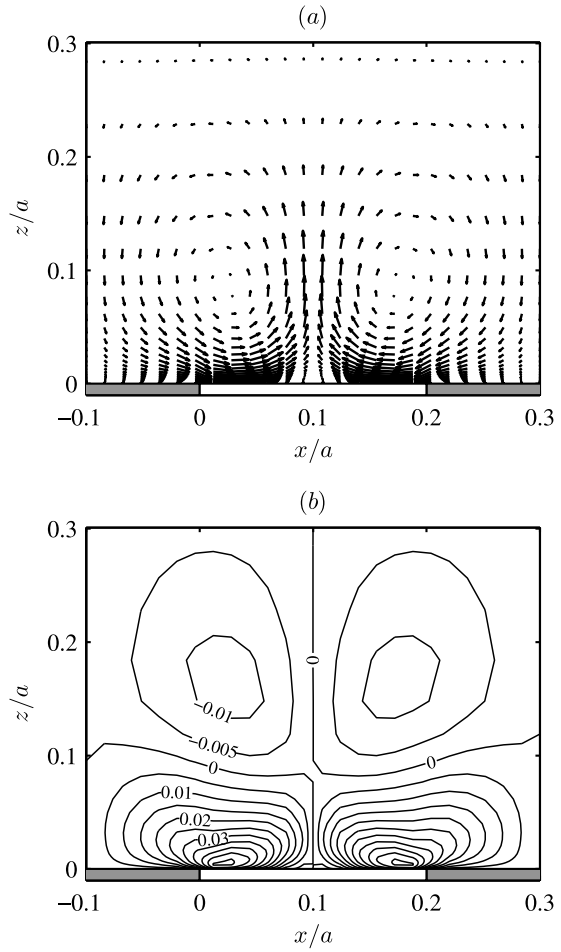

Figure 23. Computed period-averaged (a) velocity vectors and (b) horizontal velocity contours $\langle u \rangle / U_{1m}$ for an oscillatory wave boundary simulation with $a/k_N = 20$, $k_N/k'_N = 100$, $\theta = 90°$, and $\lambda/k_N = 0$, where the variable roughness strips have width $b/a = 0.2$. The shaded and unshaded regions depict the respective locations of larger and smaller roughness. This plot is to scale, with results reflected periodically in the x-direction for presentation purposes.

ated over a rougher section will tend to prohibit settling of finer grained sediments there. Induced transverse streaming towards lower roughness, as predicted here for sufficiently large θ, would additionally tend to transport suspended finer sediments away from rougher sections. As this phenomenon would tend to reinforce, rather than smooth out, spatial variations in bottom roughness, it is therefore proposed as a potential natural mechanism for transverse grain sorting within wave boundary layer flows over graded sediments.

[51] It is relevant to mention that similar roughness-induced secondary flows are known to occur within steady boundary layers. These have been used to explain the occurrence of graded bed forms e.g. so-called sand ribbons (also called sand ridges) by *McLean* [1981], *Colombini* [1993], *Colombini and Parker* [1995], *McLelland et al.* [1999], and *Wang and Cheng* [2005, 2006]. Hence, the predicted phenomenon would seem to be in close analogy to known features within steady flows. These references regarding steady flows have typically found preferential development of secondary circulation cells with characteristic size the order of the flow depth. For example, *McLean* [1981] found a preferred ratio of sand ribbon spacing to water depth of $b/D \approx 4$. By analogy, for oscillatory flows as studied herein, it is natural to wonder if this mechanism may promote similar features with characteristic size the order of the oscillatory wave boundary layer thickness δ. This possibility will be investigated in the present section.

[52] For this purpose we will complete our numerical study by considering a repeat of the simulation depicted in Figure 20b, having $a/k_N = 20$, $k_N/k'_N = 100$, $\lambda/k_N = 0$, and $\theta = 90°$, with $D/a = 1$. We will now, however, utilize a much shorter width of the periodically-connected uniform-roughness sections, compared to the intentionally large $b/a = 3$ used previously. From physical reasoning, within an oscillatory flow one might expect the preferential development of such periodically-connected strips comparable in width to the transverse extent of the strong secondary flows. Such a configuration would then allow the previously hypothesized grading mechanism to act constructively from two sides. Based on the approximate extent of the $\langle u \rangle / U_{1m} = 0.05$ contour in Figure 20b, we will therefore consider a case with $b/k_N = 4$ (i.e. $b/a = 0.2$), as an example. Note that this shorter width is comparable in magnitude to the oscillatory boundary layer thickness δ for the specified parameters. For example, (26) predicts $\delta/a = 0.052$, hence yielding $b/\delta \approx 4$. This is in line with the analogous b/D ratio for steady flows [*McLean*, 1981] mentioned above.

[53] The computed period-averaged velocities in the transverse-vertical x-z plane for this case are presented in Figure 23. Figure 23a presents computed period-averaged velocity vectors, whereas Figure 23b provides contours of the period-averaged transverse velocities $\langle u \rangle / U_{1m}$. As can clearly be seen, under the present configuration, the model predicts circulation cells to arise, with near bed flow in the direction of the less-rough section, as expected. Consistent with the analogy to steady flows, the circulation cells have a characteristic size the order of the boundary layer thickness i.e. $b \approx 4\delta \approx 0.2a$. Hence, this example supports the notion that the these secondary features predicted within oscillatory flows have close analogy to similar features known to occur within steady flows.

[54] As experimental confirmation of this phenomenon within oscillatory flows awaits, the present predictions cannot, at present, be directly tested against measurements. However, again making use of the analogy to steady flows discussed above, a comparison against similar roughness-induced secondary circulation cells in steady open channel flow, as measured recently by *Wang and Cheng* [2006], is provided in Appendix B. There it can be seen that the present model reproduces these secondary features with good qualitative, and reasonable quantitative accuracy.

7. Conclusions

[55] This work presents a comprehensive numerical study of oscillatory wave boundary layer flows over spatially varying bottom roughness, utilizing an incompressible Reynolds-averaged Navier-Stokes equation model coupled with k-ω turbulence closure, modified in a simple way to incorporate anisotropic turbulent normal stresses in line with known boundary layer characteristics at the uniform-flow

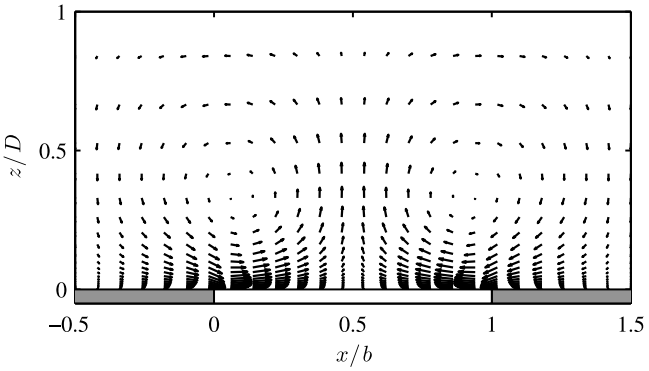

Figure B1. Computed velocity vectors showing secondary circulation cells for steady current case S75 of *Wang and Cheng* [2006], with $\theta = 0°$. The shaded and unshaded regions at the bottom depict the respective location of rough and smooth patches. Results have been reflected periodically in the x-direction for presentation purposes.

limit. The model has first been validated for bed shear stresses, turbulence characteristics, and period-averaged horizontal streaming velocities (towards larger roughness) against experimental measurements from *Fredsøe et al.* [1993], involving turbulent wave boundary layers over a sudden change in bottom roughness, as conducted in an oscillating tunnel facility.

[56] The validated model has subsequently been used to conduct a parametric study, with particular focus on the bed shear stress amplifications and maximum period-averaged horizontal streaming velocities induced by spatially varying bottom roughness. For sudden roughness transitions, new design diagrams have been presented, relevant e.g. for coastal flows over stone protection layers. These can be considered as improvements to those made previously by *Laursen et al.* [1994], based on a one-dimensional Lagrangian description. The parametric study has also been extended, to include the new and related effects of gradual (linear) changes in bottom roughness. The results demonstrate that gradually varying bottom roughness can significantly reduce bed shear stress amplifications relative to those predicted for sudden roughness transitions. The induced horizontal streaming, on the other hand, can maintain considerable strength, while shifting its position towards the direction of lower roughness. This shift has been explained physically, being due to the more rapid change of the boundary layer velocity profiles when the flow is in the direction of increasing, rather than decreasing, roughness.

[57] The model has additionally been used to study the effects of changing plan flow orientation, relative to the line of roughness transition. Model results interestingly suggest that oscillatory flow parallel, rather than normal, to a line of changing roughness can give rise to secondary transverse near-bed flows in the opposite direction to those found previously, i.e. towards smaller roughness. Based on physical reasoning, as well as analogy to phenomenon known to occur within steady flows over graded sediments, this effect is proposed as a potential natural transverse grain-sorting mechanism in coastal environments. For configurations with uniform roughness strips, it has subsequently been demonstrated that this phenomenon can lead to secondary circulation cells with characteristic size the order of the boundary layer thickness. This is consistent with the analogy to steady flows, which are known to yield preferential development of similar features with characteristic size the order of the flow depth.

Appendix A: Derivation of Anisotropic Turbulent Normal Stress Model

[58] We will here derive the modified Boussinesq approximation introduced in section 2, which is intended to yield anisotropic turbulent normal stresses consistent with steady boundary layers at the uniform-flow limit. For this purpose, consider a vertically wall-bounded flow, statistically uniform in the horizontal x-y plane, with primary streamwise direction at angle θ to the x-axis. The instantaneous fluctuating velocities in the x- and y-directions can, respectively, be expressed in terms of their streamwise (u'_{st}) and transverse (u'_{tr}) components via vector decomposition:

$$u' = u'_{st}\cos\theta - u'_{tr}\sin\theta, \tag{A1}$$

$$v' = u'_{tr}\cos\theta + u'_{st}\sin\theta. \tag{A2}$$

[59] Squaring these, time-averaging, and equating the resulting expressions with those stemming from (6), leads to:

$$\overline{u'^2} = a_{(1)}k = \overline{u'^2_{st}}\cos^2\theta + \overline{u'^2_{tr}}\sin^2\theta, \tag{A3}$$

$$\overline{v'^2} = a_{(2)}k = \overline{u'^2_{tr}}\cos^2\theta + \overline{u'^2_{st}}\sin^2\theta, \tag{A4}$$

where it has been utilized that

$$\overline{u'_{st}u'_{tr}} = 0, \tag{A5}$$

i.e. for uniform-flow in the horizontal x-y (equivalently streamwise-transverse) plane, the streamwise and transverse fluctuating components will be uncorrelated. Subject to the constraint (7), the fixed $u'^2_{st}:u'^2_{tr}:w'^2 = 4{:}3{:}2$ ratios from steady uniform boundary layer flows imply: $\overline{u'^2_{st}} = 8k/9$, $\overline{u'^2_{tr}} = 2k/3$, and $a_{(3)}k = \overline{w'^2} = 4k/9$. Inserting these back into (A3) and (A4) and dividing by k then leads immediately to (8). Hence, the derived model yields anisotropic turbulent normal stresses in line with steady boundary layers at the uniform-flow limit, for arbitrary flow direction θ.

[60] Note that if isotropic values: $\overline{u'^2_{st}} = \overline{u'^2_{tr}} = \overline{w'^2} = 2k/3$ were alternatively assumed, the above procedure leads directly to the standard Boussinesq approximation, i.e. constant $a_{(i)} = 2/3$. As we modify only the $a_{(i)}$ values, shear stresses, and any additional effects of spatial non-uniformity on normal stresses, are left treated in the standard fashion.

Appendix B: Roughness-Induced Secondary Flows in a Steady Current

[61] For further validation of the model with respect to prediction of secondary currents, we will here present a brief comparison against recent measurements by *Wang and Cheng* [2006], who investigated roughness-induced sec-

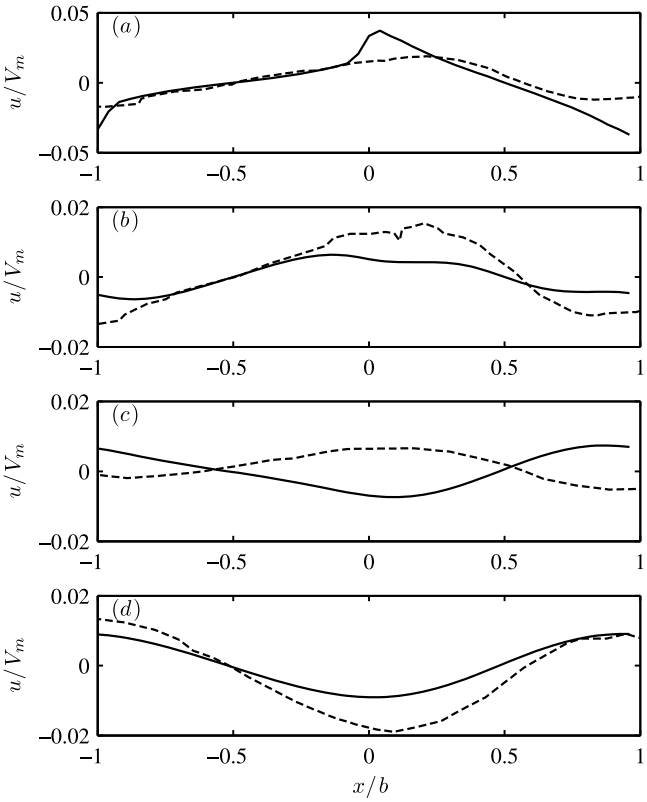

Figure B2. Comparison of computed (full lines) and measured (dashed lines) transverse velocity profiles for steady current case S75 of *Wang and Cheng* [2006] at (a) z/D = 0.0133, (b) 0.267, (c) 0.533, and (d) 0.933.

ondary circulations within steady open channel flows. Specifically, we will consider their case S75, which consisted of a series of alternating rough (grain diameter d = 0.00255 m) and smooth transverse strips of width $b = 0.075$ m, on a flow depth $D = b = 0.075$ m, with slope $S = 0.0012$. The present model setup consists of one rough and one smooth patch, connected laterally by periodic conditions, analogous to the oscillatory flow setups used throughout the paper. The top boundary is again modeled as a frictionless rigid lid. The roughness k_N = 0.00357 m (= 1.4d) is used for the rough section. When a constant body force $B_2 = Sg = 0.0118$ m/s^2 (where g = 9.81 m/s^2) is imposed in the pure y-direction (hence θ = 90°), this setup yields a steady-state cross-sectionally averaged streamwise velocity of V_m = 0.47 m/s, which matches the reported experimental value for this case.

[62] The alternating rough and smooth strips promote secondary circulation cells, qualitatively in line with those observed experimentally, having size the order of the flow depth, and with near bed transverse flow directed towards the smoother section. These are depicted in Figure B1. From a visual comparison of Figure B1 with Figure 5 of *Wang and Cheng* [2006] it can be noted that the model underpredicts the vertical position of the circulation center ($z/D \approx$ 0.35 versus measured $z/D \approx 0.5$). For further quantitative comparison, the computed and measured transverse velocities are provided in Figure B2 at four different vertical levels: z = 0.001 m, 0.02 m, 0.04 m, and 0.07 m ($z/D \approx$ 0.0133, 0.267, 0.533, and 0.933). The match is reasonable at three of the four locations, with both model and experiments yielding secondary currents of $O(0.01V_m)$, though there are some noticeable differences. For example, the present model over-predicts the peak transverse velocity near the bed (Figure B2a), while also under-predicting the flow in the opposite direction above the center of the cell (Figure B2d). The qualitative discrepancy regarding the direction of the flow in Figure B2c (z/D = 0.533) is again due to the model under-predicting the vertical position of the vortical center, i.e. the model predicts this particular position to be above the vortical center, rather than just below.

[63] While not perfect, this comparison demonstrates the ability of the present model to predict roughness-induced secondary transverse currents with good qualitative, and reasonable quantitative (roughly within a factor 2) accuracy. We further note that when simulated with a standard Boussinesq approximation, i.e. taking $a_{(i)} = 2/3$ in (6) rather than using (8), no large-scale secondary vortices develop, consistent with experience discussed elsewhere in the paper.

[64] **Acknowledgments.** The authors wish to thank the Danish Council for Strategic Research (Sea Bed Wind Farm Interaction project, grant 2104-07-0010) and the Danish Ministry of Science, Technology and Innovation (Marine Structures of the Future project, grant 11808155-P) for providing financial support, as well as the Danish Center for Scientific Computing for providing computational resources. The first author also acknowledges helpful discussions with Jacob Hjelmager Jensen regarding secondary flows and Niels Gjøl Jacobsen regarding the use of OpenFOAM.

References

Andreopoulos, J., and D. H. Wood (1982), The response of a turbulent boundary layer to a short length of surface roughness, *J. Fluid Mech.*, *118*, 143–164.

Antonia, R. A., and R. E. Luxton (1971), The response of a turbulent boundary layer to a step change in surface roughness. Part 1. Smooth to rough, *J. Fluid Mech.*, *48*, 721–761.

Antonia, R. A., and R. E. Luxton (1972), The response of a turbulent boundary layer to a step change in surface roughness. Part 2. Rough to smooth, *J. Fluid Mech.*, *53*, 737–757.

Bayazit, M. (1976), Free surface flow in a channel of large relative roughness, *J. Hydraul. Res.*, *14*, 115–126.

Bayazit, M. (1983), Flow structure and sediment transport mechanics in steep channels, in *Euromech 156: Mechanics of Sediment Transport*, edited by B. M. Sumer and A. Muller, pp. 197–206, A. A. Balkema, Rotterdam, Netherlands.

Belcher, S. E., D. P. Xu, and J. C. R. Hunt (1990), The response of a turbulent boundary layer to arbitrarily distributed two-dimensional roughness changes, *Q. J. R. Meteorol. Soc.*, *116*, 611–635.

Beljaars, A. C. M., J. L. Walmsley, and P. A. Taylor (1990), A mixed spectral finite difference model for neutrally stratified boundary layer flow over roughness changes and topography, *Boundary Layer Meteorol.*, *38*, 273–303.

Blom, J., and L. Wartena (1969), The influence of changes in surface roughness on the development of a turbulent boundary layer in the lower atmosphere, *J. Atmos. Sci.*, *26*, 255–265.

Chan, A. T. (2001), Atmospheric turbulent boundary layer development due to a change in surface roughness, *Int. J. Eng. Sci.*, *39*, 2001–2014.

Chen, X. W., and Y. M. Chiew (2003), Response of velocity and turbulence to sudden change of bed roughness in open-channel flow, *J. Hydraul. Eng. ASCE*, *129*, 35–43.

Colombini, M. (1993), Turbulence-driven secondary flows and formation of sand ridges, *J. Fluid Mech.*, *254*, 701–719.

Colombini, M., and G. Parker (1995), Longitudinal streaks, *J. Fluid Mech.*, *304*, 161–183.

Foster, D. L., R. A. Guenther, and R. A. Holman (1999), An analytic solution to the wave bottom boundary layer governing equation under arbitrary forcing, *Ocean Eng.*, *26*, 595–623.

Fredsøe, J. (1984), Turbulent wave boundary layer in wave-current motion, *J. Hydraul. Eng. ASCE*, *110*, 1103–1120.

Fredsøe, J., and R. Deigaard (1992), *Mechanics of Coastal Sediment Transport*, World Sci., Singapore.

Fredsøe, J., B. Sumer, T. Laursen, and C. Pedersen (1993), Experimental investigation of wave boundary layers with a sudden change in roughness, *J. Fluid Mech.*, *252*, 117–145.

Fuhrman, D. R., J. Fredsøe, and B. M. Sumer (2009a), Bed slope effects on turbulent wave boundary layers: 1. Model validation and quantification of rough-turbulent results, *J. Geophys. Res.*, *114*, C03024, doi:10.1029/2008JC005045.

Fuhrman, D. R., J. Fredsøe, and B. M. Sumer (2009b), Bed slope effects on turbulent wave boundary layers: 2. Comparison with skewness, asymmetry, and other effects, *J. Geophys. Res.*, *114*, C03025, doi:10.1029/2008JC005053.

Fuhrman, D. R., M. Dixen, and N. G. Jacobsen (2010), Physically-consistent wall boundary conditions for the k-ω turbulence model, *J. Hydraul. Res.*, *48*, 793–800.

Grant, W. D., and O. S. Madsen (1979), Combined wave and current interaction with a rough bottom, *J. Geophys. Res.*, *84*, 1797–1808.

Grass, A. J. (1971), Structural features of turbulent flow over smooth and rough boundaries, *J. Fluid Mech.*, *50*, 233–255.

Holmedal, L. E., and D. Myrhaug (2009), Wave-induced steady streaming, mass transport and net sediment transport in rough turbulent ocean bottom boundary layers, *Cont. Shelf Res.*, *29*, 911–926.

Jensen, B. L., B. M. Sumer, and J. Fredsøe (1989), Turbulent oscillatory boundary layers at high Reynolds numbers, *J. Fluid Mech.*, *206*, 265–297.

Jensen, N. O. (1978), Change of surface-roughness and planetary boundary-layer, *Q. J. R. Meteorol. Soc.*, *104*, 351–356.

Justesen, P. (1988), Prediction of turbulent oscillatory flow over rough beds, *Coastal Eng.*, *12*, 257–284.

Laursen, T. S., J. Fredsøe, and B. M. Sumer (1994), Numerical prediction of wave boundary layer over a bed with a change in roughness, *Coastal Eng.*, *24*, 81–96.

Lundgren, H., and I. G. Jonsson (1961), Bed shear stress induced by a wave motion, *Basic Res. Prog. Rep., 1*, pp. 3–5, Coastal Eng. Lab., Tech. Univ. of Denmark, Kongens Lyngby.

McLean, S. R. (1981), The role of non-uniform roughness in the formation of sand ribbons, *Mar. Geol.*, *42*, 49–74.

McLelland, S. J., P. J. Ashworth, J. L. Best, and J. R. Livesey (1999), Turbulence and secondary flow over sediment stripes in weakly bimodal bed material, *J. Hydraul. Eng. ASCE*, *125*, 463–473.

Myrhaug, D. (1982), On a theoretical-model of rough turbulent wave boundary-layers, *Ocean Eng.*, *9*, 547–565.

Myrhaug, D., and O. H. Slaattelid (1989), Combined waves and current boundary layer model for fixed rough seabeds, *Ocean Eng.*, *16*, 119–142.

Rao, K. S., J. C. Wyngaard, and O. R. Cote (1974), The structure of the two-dimensional internal boundary layer over a sudden change of surface roughness, *J. Atmos. Sci.*, *31*, 738–746.

Roulund, A., B. M. Sumer, J. Fredsøe, and J. Michelsen (2005), Numerical and experimental investigation of flow and scour around a circular pile, *J. Fluid Mech.*, *534*, 351–401.

Schofield, W. H. (1975), Measurements in adverse-pressure-gradient turbulent boundary-layers with a step change in surface-roughness, *J. Fluid Mech.*, *70*, 573–593.

Shir, C. C. (1972), A numerical computation of air flow over a sudden change in surface roughness, *J. Atmos. Sci*, *29*, 304–310.

Sleath, J. F. A. (1987), Turbulent oscillatory flow over rough beds, *J. Fluid Mech.*, *182*, 369–409.

Sleath, J. F. A. (1988), Transition in oscillatory flow over rough beds, *J. Waterw. Port C ASCE*, *114*, 18–33.

Speziale, C. G. (1982), On turbulent secondary flows in pipes of non-circular cross-section, *Int. J. Eng. Sci.*, *20*, 863–872.

Speziale, C. G. (1987), On nonlinear k-l and k-ε models of turbulence, *J. Fluid Mech.*, *178*, 459–475.

Sumer, B. M., T. S. Laursen, and J. Fredsøe (1993), Wave boundary layer in a convergent tunnel, *Coastal Eng.*, *20*, 317–342.

Sumer, B. M., L. H. C. Chua, N.-S. Cheng, and J. Fredsøe (2003), Influence of turbulence on bed load sediment transport, *J. Hydraul. Eng. ASCE*, *129*, 585–596.

Taylor, P. A. (1969), The planetary boundary layer around a change in surface roughness, *J. Atmos. Sci.*, *26*, 432–440.

Townsend, A. A. (1966), The flow in a turbulent boundary layer after a sudden change in surface roughness, *J. Fluid Mech.*, *26*, 255–266.

Wang, Z.-Q., and N.-S. Cheng (2005), Secondary flows over artificial bed strips, *Adv. Water Resour.*, *28*, 441–450.

Wang, Z.-Q., and N.-S. Cheng (2006), Time-mean structure of secondary flows in open channel with longitudinal bedforms, *Adv. Water Resour.*, *29*, 1634–1649.

Wilcox, D. C. (2006), *Turbulence Modeling in CFD*, 3rd ed., DCW Ind., Inc., La Canada, Calif.

Wilcox, D. C. (2008), Formulation of the k-ω turbulence model revisited, *AIAA J.*, *46*, 2823–2838.

Wright, S. D., L. Elliott, D. B. Ingham, and M. J. C. Hewson (1998), The adaptation of the atmospheric boundary layer to a change in surface roughness, *Boundary Layer Meteorol.*, *89*, 175–195.

Zou, Q., and A. E. Hay (2003), The vertical structure of the wave bottom boundary layer over a sloping bed: Theory and field measurements, *J. Phys. Oceanogr.*, *33*, 1380–1400.

Zou, Q., A. E. Hay, and A. J. Bowen (2003), Vertical structure of surface gravity waves propagating over a sloping seabed: Theory and field measurements, *J. Geophys. Res.*, *108*(C8), 3265, doi:10.1029/2002JC001432.

J. Fredsøe, D. R. Fuhrman, and B. M. Sumer, Department of Mechanical Engineering, Technical University of Denmark, Nils Koppels Alle, Bldg. 403, DK-2800 Kongens Lyngby, Denmark. (jf@mek.dtu.dk; drf@mek.dtu.dk; bms@mek.dtu.dk)